



This is a repository copy of *Hemodynamic parameters that may predict false-lumen growth in type-B aortic dissection after endovascular repair: A preliminary study on long-term multiple follow-ups.*

White Rose Research Online URL for this paper:

<https://eprints.whiterose.ac.uk/122934/>

Version: Accepted Version

Article:

Xu, H., Li, Z., Dong, H. et al. (6 more authors) (2017) Hemodynamic parameters that may predict false-lumen growth in type-B aortic dissection after endovascular repair: A preliminary study on long-term multiple follow-ups. *Medical Engineering & Physics*, 50. pp. 12-21. ISSN 1350-4533

<https://doi.org/10.1016/j.medengphy.2017.08.011>

Reuse

This article is distributed under the terms of the Creative Commons Attribution-NonCommercial-NoDerivs (CC BY-NC-ND) licence. This licence only allows you to download this work and share it with others as long as you credit the authors, but you can't change the article in any way or use it commercially. More information and the full terms of the licence here: <https://creativecommons.org/licenses/>

Takedown

If you consider content in White Rose Research Online to be in breach of UK law, please notify us by emailing eprints@whiterose.ac.uk including the URL of the record and the reason for the withdrawal request.



eprints@whiterose.ac.uk
<https://eprints.whiterose.ac.uk/>

Hemodynamic Parameters That May Predict False-lumen Growth in Type-B Aortic Dissection after Endovascular Repair: A Preliminary Study on Long-term Multiple Follow-ups

Huanming Xu^{1,2}, Zhenfeng Li^{1,2}, Huiwu Dong³, Yilun Zhang¹, Jianyong Wei¹, Paul N. Watton^{5,6}, Wei Guo⁷, Duanduan Chen^{1,2*}, Jiang Xiong^{7*}

¹School of Life Science, Beijing Institute of Technology, China

²Key Laboratory of Convergence Medical Engineering System and Healthcare Technology, The Ministry of Industry and Information Technology, Beijing Institute of Technology, China

³Department of Ultrasound Diagnosis, Chinese PLA General Hospital, China

⁵Department of Computer Science & INSIGNEO Institute, University of Sheffield, UK

⁶Department of Mechanical Engineering and Material Science, University of Pittsburgh

⁷Department of Vascular and Endovascular Surgery, Chinese PLA General Hospital, China

***Corresponding author:** Prof Duanduan Chen

School of Life Science, Beijing Institute of Technology, Beijing,
100081, China.

Tel. +86-10-68912154

Email. duanduan@bit.edu.cn

Dr Jiang Xiong

Department of Vascular and Endovascular Surgery,
Chinese PLA General Hospital, Beijing, 100853, China.

Tel. +86-10-66938349

Email. xiongjiangdoc@126.com

1 **ABSTRACT**

2 Thoracic endovascular aortic repair (TEVAR) is commonly applied in type-B aortic
3 dissection. For patients with dissection affects descending aorta and extends downward to
4 involve abdominal aorta and possibly iliac arteries, false lumen (FL) expansion might occur
5 post-TEVAR. Predictions of dissection development may assist in medical decision on
6 re-intervention or surgery. In this study, two patients are selected with similar morphological
7 features at initial presentation but with different long-term FL development post-TEVAR
8 (stable and enlarged FL). Patient-specific models are established for each of the follow-ups.
9 Flow boundaries and computational validations are obtained from Doppler ultrasound
10 velocimetry. By analyzing the hemodynamic parameters, the false-to-true luminal pressure
11 difference (PDiff) and particle relative residence time (RRT) are found related to FL
12 remodeling. It is found that (i) the position of the first FL flow entry is the watershed of
13 negative-and-positive PDiff and, in long-term follow-ups, and the position of largest PDiff is
14 consistent with that of the greatest increase of FL width; (ii) high RRT occurs at the FL
15 proximal tip and similar magnitude of RRT is found in both stable and enlarged cases; (iii)
16 comparing to the RRT at 7days post-TEVAR, an increase of RRT afterwards in short-term is
17 found in the stable case while a slight decrease of this parameter is found in the enlarged case,
18 indicating that the variation of RRT in short-term post-TEVAR might be potential to predict
19 long-term FL remodeling.

20

21 **Key Words:** aortic dissection; hemodynamics; endovascular procedures.

22 INTRODUCTION

23 Aortic dissection (AoD) is a severe cardiovascular disease, where a surge of blood
24 flowing into the aortic wall via an initial tear or damage of the intima and splitting the
25 single aortic lumen into a true and false lumen (TL and FL). Stanford type-B AoD
26 indicates those with the dissection begins distal to the supraaortic branches.
27 Interventional treatment of Stanford type-B AoD commonly involves thoracic
28 endovascular aortic repair (TEVAR)[1]. In a number of patients, FL expansion is
29 found post-TEVAR, especially in the infrarenal aorta. Recent study confirmed that
30 abdominal aortic expansion can be frequently found after TEVAR and is independent
31 from thoracic FL thrombosis[2]. Prediction of FL growth may contribute to early
32 decision-making of re-intervention or surgery. The post-TEVAR development of
33 dissection is highly dependent on local hemodynamics[3]. Medical imaging tools such
34 as Doppler ultrasound[4] and phase-contrast MR (pcMR)[5] are able to capture the
35 flow velocity within aorta. However, the former provides velocity information at a
36 certain position of the vessel, and the latter reveals flow movement with relatively low
37 spatial and temporal resolution[6, 7]. On the other hand, the uptake of
38 ^{18}F -fluorodeoxyglucose in PET-CT can indicate complications in AoD[8] and positive
39 correlation between the uptake and wall shear stress is found in aortic aneurysm
40 study[9]; however, PET-CT is relatively expensive and the flow information cannot be
41 directly reported. Thus, computational simulations that can provide hemodynamic
42 parameters, such as flow, pressure and shear stress distributions, may enrich analysis.

43 Previous computational works focusing on type-B AoD include investigations on
44 hemodynamic features[10-14], luminal flow exchange[12, 15], post-TEVAR flow
45 effects[16-18], tear-induced flow effects[19, 20] and fluid-structure interaction
46 studies[21, 22]. Besides, 4D pcMR[5, 23] and phantom[24, 25] measurements have been
47 conducted to compare with or validate the computed results. In this study, we
48 investigate the flow-driven dissection development after TEVAR based on long-term
49 multiple follow-ups. Flow conditions in patients with stable and enlarged FL are
50 compared and key hemodynamic parameters that are related to dissection growth in
51 abdominal aorta are proposed, facilitating medical decision-making on post-TEVAR
52 treatment.

53

54

55 **METHODS**

56 *Image Acquisition and Model Reconstruction*

57 This study was approved by the institutional review board of the Chinese PLA
58 General Hospital. Written informed consent was obtained from the patients involved
59 in this study. Two male patients (PI and PII) with subacute Stanford type-B AoD
60 underwent arterial-phase CT angiography (CTA) at initial presentation and during the
61 follow-up examinations after TEVAR via a dual-source CT scanner (SOMATOM
62 Definition Flash, SIEMENS, Germany). Details of the CTA scan and the patient
63 information are described in S1, Supporting Document. Image segmentation and
64 surface reconstruction of AoD were conducted through Mimics (Materialise,
65 Belgium). The cross-sectional contours of the reconstructed geometries were mapped
66 back to CTA images to ensure that the 3D models present the actual outline of the
67 vessel lumen. Detailed views of the models are shown in Fig.1, where PI/II-1
68 indicates the models pre-TEVAR while PI/II-2 and others are models post-TEVAR.
69 After TEVAR, PI and PII have experienced six- (7days~53months) and four-times
70 (7days~35months) CTA scans. The FL in PI was in stable condition (PI-2~7, Fig.1b)
71 while that in PII was expanding (PII-2~5, Fig.1d). The models were meshed in ICEM
72 (ANSYS Inc, Canonsburg, USA) with tetrahedral elements in the core region and
73 prismatic cells (10 layers) in the boundary layer near the aortic wall. The grid
74 resolution varies from 2,564,019 to 3,153,829 cells.

75

76 *Doppler Ultrasound and Boundary Conditions*

77 Time-variant velocities at ascending aorta (AAo), brachiocephalic trunk (BT), left
78 common carotid artery (LCCA), left subclavian artery (LSA) were measured via
79 Doppler ultrasound of the patients, and velocity variation at the distal thoracic aorta
80 (DTAo, about 5cm above celiac trunk) was measured in the final examination of PI to
81 provide validation of the computational results. This is because the true lumen (TL)
82 remodeling at this position in PI is sufficient, so that relatively organized flow is
83 found and the central line of vessel can be accurately identified. The velocity of AAo
84 was measured through the apical 5-chamber view and the suprasternal long axis view
85 of aortic arch. The two results were compared to ensure the maximum velocity at
86 AAo could be captured. For other arteries (BT, LCCA, LSA and DTAo), Doppler

87 velocimetry has been conducted at the proximal and distal sites of the targeted
88 measurement vessel. Mean velocity over a cardiac cycle at the two sites for each
89 particular vessel was then calculated and compared. When the difference between
90 them is less than 5%, the measured velocity is considered effective. Details of the
91 measurement are described in S2, Supporting Document.

92 The upper edge of the velocity sonogram was extracted (Fig.1e) as the variation of
93 the maximum velocity at the measured site. The flow rates at AAo, BT, LCCA and
94 LSA, as the velocity boundary conditions, can then be calculated based on the
95 measured time-variant maximum velocity and the assumed flat flow profile for AAo
96 and parabolic flow profile for the others. The velocity boundary conditions of the
97 models is shown in Fig.S1a, Supporting Document. Pulsatile waveforms of the
98 pressure at celiac artery (CA), superiormesenteric artery (SMA), renal arteries and the
99 outlets at common iliac arteries were obtained from previous study[26] (Fig.S1b,
100 Supporting Document). As shown in Fig.1, two models in PII (PII-1 and PII-4) were
101 cropped below the iliac bifurcation due to the relatively shorter CT scanning range. To
102 eliminate the outlet effects, time-variant pressure distribution at the cropping plane
103 has been calculated in PII-2~3 and PII-5. The averaged pressure information at this
104 cropping plane was mapped to PII-1 and PII-4, serving as the pulsatile pressure
105 outlets.

106

107 *Numerical Models*

108 The vessel wall was assumed as no-slip and rigid, due to low distensibility in
109 long-term follow-ups[27]. The blood was treated as Newtonian and incompressible
110 with density of 1044kg/m^3 and dynamic viscosity of $0.00365\text{kg}\cdot\text{m}^{-1}\cdot\text{s}^{-1}$ [28]. The
111 average Reynolds number over a cardiac cycle, calculated based on the equivalent
112 diameter ($D_e = 2\sqrt{\text{Area}/\pi}$) and velocity at the inlet of the ascending aorta in PI and
113 PII, were between 2066-2197 and 2844-2960, respectively. Our previous study
114 confirmed that laminar simulations with adequately fine mesh resolutions, especially
115 refined near the walls, can capture flow patterns as turbulence model[15]. To further
116 confirm this, we solved the flow in the first follow-up cases (PI-2 and PII-2) by both
117 laminar and $k-\omega$ SST turbulence models, where the flow in the abdominal aortic
118 region is the fastest during the follow-ups. Similar flow patterns were found and the
119 discrepancy of the maximum velocity and wall shear stress (WSS) in the abdominal

120 aorta was 4.2% and 5.2% respectively (the laminar and turbulent results of PII-2 were
121 shown in Fig.S2, Supporting Document), ensuring the rationality of laminar model to
122 be applied in the current problem. A finite volume solver, CFD-ACE+ (ESI Group,
123 France) was employed. The heart-beat cycle of the patients was measured at each
124 clinical examination. The averaged cardiac cycle for PI and PII were 71 and
125 69beat/min respectively. Temporal discretization of numerical models was assigned as
126 45step/cycle. Simulation was carried out for 5 cardiac cycles to achieve a periodic
127 solution and results of the final cycle were presented. Grid and temporal
128 independency analyses on finer grids and finer temporal discretizations were
129 conducted to ensure the base resolution with the base time step settings are adequate
130 (S3, Supporting Document).

131

132 **RESULTS**

133 *Aortic Remodeling*

134 Aortic remodeling was assessed by: (i) size and numbers of the aortic tears (AoT), (ii)
135 change of luminal volume, and (iii) growth of aortic diameter. There are four major
136 AoTs along the aorta for both patients at initial presentation. The primary entry
137 (AoT-1) in both patients is located at the proximal region of descending aorta and the
138 locations of other AoTs (AoT-2~4) are displayed in Fig.1. After TEVAR, the primary
139 entry was sealed and after the first follow-up of PI, AoT-2 was disappeared.
140 Considering the position and local aortic curvature of the tears, AoT-4 is the exit of
141 the flow from FL to TL, while the function of AoT-2 and AoT-3 is uncertain. Since
142 only the flow entries towards the FL is able to bring mechanical impact into the
143 dissection, size measurement was only performed on AoT-2 and AoT-3 (Table 1).
144 Post-TEVAR, both AoT-2 and AoT-3 in PI and PII are enlarged, probably due to the
145 greater flow impact on these sites after AoT-1 was sealed.

Table 1. The size of the aortic tears in the patients with long-term follow-ups

Tear	Geometry	PI-1	PI-2	PI-3	PI-4	PI-5	PI-6	PI-7
AoT-2	H[mm]	7.87	7.15	-	-	-	-	-
	W[mm]	8.97	10.76	-	-	-	-	-
	A[mm ²]	64.61	70.71	-	-	-	-	-
AoT-3	H[mm]	13.86	18.79	17.93	15.31	18.23	8.81	8.57
	W[mm]	10.04	9.38	6.03	8.90	7.30	6.72	5.75
	A[mm ²]	116.13	150.82	106.40	119.19	128.82	93.49	44.09
Tear	Geometry	PII-1	PII-2	PII-3	PII-4	PII-5		
AoT-2	H[mm]	8.17	8.41	5.74	11.04	11.20		
	W[mm]	9.34	9.96	7.36	9.59	6.03		
	A[mm ²]	62.61	70.47	37.33	89.50	54.05		
AoT-3	H[mm]	9.91	9.55	7.77	6.25	6.19		
	W[mm]	10.01	11.47	9.34	8.04	9.90		
	A[mm ²]	85.27	99.32	61.51	40.35	53.32		

H-Height; W-Width; A-Area.

146

147 The change of luminal volume is shown in Fig.2. The volume of TL (V_{TL}) involves
148 the initial dissection-affected TL region, while $V_{TL-Part}$ indicates the
149 dissection-affected TL region during the follow-ups. Variations of V_{TL} , volume of FL
150 (V_{FL}) and the ratio between $V_{TL-Part}$ and V_{FL} are displayed in Fig.2b. V_{FL} in the stable
151 case (PI) reduces gradually post-TEVAR, except for the final examination, where a
152 trivial increase of V_{FL} is found (131.6mm³ in 20months). However, V_{FL} in the
153 expanding case (PII) reduces in the first two follow-ups but enlarges afterwards,
154 where the V_{FL} growths in PII-4 and PII-5 are 2,138mm³ and 34,989mm³ respectively,
155 the durations of which are both 17months (Fig.2b). For both cases, the TL-to-FL
156 volume ratio ($V_{TL-Part}/V_{FL}$) keeps increasing, except for PI-6 and PII-3 (pointed by
157 arrows). This is because significant FL regression occurs at the proximal region (blue
158 squares in Fig.1b,1d), which shortens the comparison region. Since TL remodeling is
159 insufficient in this region, value of $V_{TL-Part}/V_{FL}$ reduces. The averaged increase rates of
160 $V_{TL-Part}/V_{FL}$ in the follow-ups of PI and PII are 1.8% and 0.3% per month,
161 respectively, indicating a significant luminal remodeling difference.

162 The aortic diameter (D) is measured in each model, taking into account the width of
163 TL and FL (W_{TL} and W_{FL}) and the thickness of flap. As shown in Fig.1f,
164 measurements have been conducted in the axial plane of the CTA datasets, along a
165 line that crosses the centre of the flap and is perpendicular to the flap. Four
166 measurement positions are selected in the abdominal aorta. As shown in Fig.2a, they
167 are 1cm below diaphragm (L1), 1cm above CA (L2), 3.5cm below SMA (L3) and 9cm
168 below SMA (L4). Fig.2c~e display the variation of D, W_{TL} and W_{FL} respectively.
169 Positive TL remodeling is found in PI and PII in general, except for L3 and L4 in PI-3

170 and L3 in PII-4~5. W_{FL} at the proximal region of PI (L1 and L2) reduces greatly
171 during the follow-up, while in the distal region (L3 and L4), variation of W_{FL} is stable.
172 In PII, W_{FL} increases sharply since the second follow-up (PII-3). Comparing the
173 variation of W_{TL} , W_{FL} and D , it can be found that the variation pattern of D is mainly
174 determined by the variation of W_{FL} .

175

176 *Flow Pattern, Validation and Luminal Flow Exchange*

177 Fig.3 shows the flow streamlines at systolic peak where the color map of velocity
178 magnitude is restricted to a certain range in PI (0~2.51m/s) and PII (0~3.78m/s) to
179 assist visualization of the longitudinal velocity variation. At systolic peak, fast and
180 organized flow is found in TL; while vortical and relatively slow flow presents in FL.
181 Highest velocity presents in the short-term follow-ups (PI-2~3, 4months for PI;
182 PII-2~3, 1months for PII) at the region below stentgraft and above AoT-2 and -3,
183 where TL remodeling is insufficient and the blood has not been diverted. In long-term
184 follow-ups (PI-4~7 and PII-4~5), the flow in the proximal FL is generally slow
185 (<0.5mm/s); while below AoT-2 (the first re-entry), where blood perfusion occurs,
186 faster flow up to 1.53m/s in PI and 2.22m/s in PII are found in the FL with helical
187 feature (Fig.3c).

188 To validate the computational results, Doppler ultrasound velocimetry was
189 performed at distal thoracic aorta (5cm above CA) along the centerline of TL. This
190 was only conducted at the final examination of PI, because its TL in the distal thoracic
191 aorta is fully remodeled and the local flow is therefore organized (Fig.3a). The
192 measured and computed velocities at the centre of the cross-section of the vessel, 5cm
193 above CA, are 1.58m/s and 1.66m/s respectively, indicating a difference of 5.1%.
194 Moreover, the computed velocity variation pattern is similar to the measured one
195 (Fig.S3, Supporting Document), ensuring the rationality of computational results.

196 Fig.4 displays the luminal flow exchange via the primary entry for initial
197 presentation and that via AoT-2 and AoT-3 during the follow-ups. As
198 abovementioned, AoT-4 functions as the outlet of FL throughout the cardiac cycle,
199 thus it is not displayed in Fig.4. As shown in Fig.4a (positive values indicates flow
200 enters FL), before treatment, the TL-to-FL flow exchange in PI and PII presents
201 similar pattern: the primary entry serves as the main flow inlet of FL; AoT-2 functions
202 as the outlet of FL in the initial part of systole and behaves as inlet in the rest part of

203 cardiac cycle; and AoT-3 mainly serves as the outlet of FL. There are 31.48% and
204 40.00% of the total flow diverted to FL over a cardiac cycle for PI and PII
205 respectively, at initial presentation. After TEVAR, the function of the tears changes. In
206 PI, AoT-2 becomes the inlet of FL in the entire heart-beat cycle (Fig.4b), while AoT-3
207 functions as the inlet of FL during systole and serves as the outlet in diastole (Fig.4c).
208 Since the second follow-up of PI, AoT-2 is closed and AoT-3 gradually becomes the
209 inlet of FL throughout the entire cardiac cycle. The flow entering FL are 16.67%,
210 6.98%, 8.24%, 9.59%, 5.43%, 3.09% of the total flow for case PI-2~7 respectively,
211 the variation of which is consistent to the variation of tear size (Table 1) and it is
212 generally reducing. In PII, both of AoT-2 and AoT-3 are existed during the follow-ups.
213 AoT-2 mainly serves as the inlet of FL; especially in model PII-4 and PII-5, positive
214 values of mass flow rate are found in the entire cardiac cycle (Fig.4b). AoT-3 diverts a
215 small amount of flow into the FL during systole and mainly behaves as the outlet of
216 FL (Fig.4c). There are 5.22%, 3.06%, 14.76% and 10.23% of the total flow diverted
217 into FL in case PII-2~5 respectively, the variation of which is also consistent with the
218 variation of tear size.

219

220 *Loading Distribution along the Aorta*

221 Fig.5a~b display the pressure drop at systolic peak (PD_{sys}, the difference between the
222 local pressure and the pressure at the bottom of the model). In TL, PD_{sys} reduces
223 from the inlet of AAo to the outlets of common iliac arteries. At initial presentation
224 (PI-1 and PII-1), FL diverts part of the total flow (31.48% for PI and 40.00% for PII),
225 maintaining PD_{sys} in relatively low values. After TEVAR, in short-term follow-ups
226 (PI-2~3 and PII-2~3), proximal descending aorta is supported by stentgraft and
227 reshaped; however, below the endograft, TL remains collapsed, inducing larger
228 resistance and resulting in higher velocity and regional lower pressure in this region
229 (indicated by arrows in Fig.5a~b). In long-term follow-ups (PI-4~7 and PII-4~5), TL
230 remodeling in distal thoracic aorta is improved; PD_{sys} thus gradually reduces along
231 aorta. In contrary, PD_{sys} in FL is relatively uniform, which is probably due to the
232 higher energy exchange induced by the vortical flow. Fig.5d shows the variation of
233 the maximum PD_{sys} during the follow-ups. For both patients, the maximum PD_{sys}
234 increases greatly soon after TEVAR (7days); along with the progress of TL
235 remodeling, the maximum PD_{sys} reduces. The PD_{sys} in normal aorta model (Fig.5c)

236 based on the same boundary conditions as PI and PII is also computed and the
237 averaged maximum PD_{sys} is shown by the dash line in Fig.5d. Since the growth of
238 FL in the two patients shows obvious difference, the similar variation pattern of
239 PD_{sys} indicates that the pressure drop is mainly affected by TL remodeling.

240 The mean arterial pressure drop (PD_{mean}) from AAO to the common iliac arteries
241 during a cardiac cycle is also calculated. It is 6.29mmHg for the initial model of PI
242 and 4.70mmHg for the final model (53months post-TEVAR), which is slightly higher
243 than that in normal aorta for the studied segment (4mmHg[29]). The PD_{mean} of PII at
244 the initial and final (35months post-TEVAR) models are 6.53mmHg and 6.07mmHg,
245 respectively, consistent with its insufficient TL remodeling.

246 In the final examination of PI (PI-7), V_{FL} is slightly increased, D and W_{FL} also
247 increase at L3 (Fig.2); however, the flow exchange and tear size at this stage are both
248 reduced. Fig.5e displays the pressure distribution at systolic peak (P_{sys}) on a slice of
249 FL for PI-6~7. It shows that the smaller tear size reduces the flow entering FL,
250 however, it increases the velocity and induces higher pressure impact on the outer
251 wall of FL (indicated by arrows in Fig.5e). The highest pressure of the impact region
252 in PI and PII at final examination are 114.37 and 115.41mmHg respectively. Besides,
253 by blanking the region with P_{sys}<109.15mmHg, which is the 95% of the averaged
254 maximum pressure in PI and PII at final examination, Fig.5f shows that the high
255 pressure region (in red) in the FL of PII is much larger than that in PI. In fact, the FL
256 growth rates of PI and PII at the final examination are 0.22mm³/day and
257 68.61mm³/day respectively.

258

259 *Luminal Pressure Difference, Wall Shear Stress and Relative Residence Time*

260 To investigate the pressure difference (PD_{diff}) between TL and FL, a series of slices
261 that are perpendicular to the centerline of TL are extracted and the net pressures in TL
262 (P_{TL}) and FL (P_{FL}) on each slice over a cardiac cycle are calculated. Fig.6 displays
263 PD_{diff} (PD_{diff}=P_{FL}-P_{TL}) in each model. In both patients, pre-TEVAR (Fig.6a,6e), P_{FL} is
264 smaller than P_{TL} at the level above AoT-2; while, below AoT-2, P_{FL} is larger than P_{TL},
265 pushing the FL towards TL. Post- TEVAR, the primary entry is closed. In PI, negative
266 values of PD_{diff} are found above AoT-3 (Fig.6b~c), indicating higher P_{TL} presents in
267 this region, which supports the aortic wall and assists in TL expansion. However, in
268 the region below AoT-3 in PI, due to the blood perfusion into the FL, positive values

269 of PDiff present, indicating FL propulsion on the TL. In the final follow-up of PI
270 (Fig.6d), the maximum value of PDiff is 0.22mmHg. This maximum PDiff occurs
271 close to L3. At this position, W_{FL} and W_{TL} increase by 1.02mm and 0.46mm
272 respectively (Fig.2), indicating this small value of PDiff (0.22mmHg) is not large
273 enough to squeeze TL but the local pressure in FL (Fig.5e) is able to induce further
274 FL expansion. On the other hand, in PII, post-TEVAR, AoT-2 becomes the main inlet
275 of the flow into FL. Higher above this tear, P_{TL} is larger than P_{FL} , supporting TL
276 expansion (Fig.6e~f). In the near region above AoT-2, TL remodeling is insufficient
277 for the short-term follow-ups but P_{FL} gradually increases; thus, regional positive PDiff
278 is found in PII-3 above AoT-2 (arrow indicated in Fig.6f). Below AoT-2, positive
279 values of PDiff dominate and the maximum PDiff in the final examination of PII is
280 1.39mmHg, more than 6-times as high as that in PI, occurring close to L3. Taking
281 account of that, in PII-5, W_{TL} decreases yet W_{FL} increases at L3 (Fig.2d~e), this high
282 PDiff propels TL collapse and the local pressure pushes FL growth.

283 Fig.7 shows the wall shear stress (WSS) distribution on the flap at systolic peak. Its
284 variation over a cardiac cycle is shown in Video S1-6, Supporting Document. In both
285 patients, the WSS on the flap at the FL side (WSS_{FL}) is significantly smaller than that
286 on the TL side (WSS_{TL}); and the WSS_{TL} in PII is generally higher than that in PI. At
287 initial presentation, the maximum WSS_{TL} occurs at the edge of primary entry; while
288 the maximum WSS_{FL} occurs at the proximal descending aorta along the side opposite
289 to the primary entry (indicated by arrows in Fig.7b). In follow-ups, the maximum
290 WSS_{TL} occurs at the region where TL presents most collapse; while the maximum
291 WSS_{FL} occurs at the edge of the tears. AoT-3 and AoT-2 are the main FL flow entries
292 for PI and PII in follow-ups, which induces helical flow in the downstream and high
293 WSS_{FL} on the side opposite to the tears (indicated by hollow arrows in Fig.7b). To
294 further visualize the variation of WSS_{FL} at different regions along the flap on the FL
295 side, the color map is assigned to 0~5Pa (Fig.7c) and 0~0.5Pa (Fig.7d) to show the
296 distal and proximal region respectively. In PI, WSS_{FL} at the region below AoT-3
297 reduces obviously from PI-4 to PI-6; however, in the final examination, it is slightly
298 increased, although the maximum WSS_{FL} in this region is still smaller than 1Pa. In
299 PII, WSS_{FL} presents obvious increase in PII-4 and reduces slightly in PII-5; the
300 maximum WSS_{FL} at the region between AoT-2 and AoT-3 in the final examination is
301 5.21Pa.

302 Particle residence time is proposed to be related to thrombosis establishment[14].

303 The relative residence time (RRT), which is based on the time-averaged WSS
304 (TAWSS) and oscillatory shear index (OSI), $[(1-2 \cdot \text{OSI}) \cdot \text{TAWSS}]^{-1}$, reflects particle
305 residence time and thus may correspond with the region of thrombosis[14, 30].
306 Fig.8a~b show the RRT distributions (normalized by the maximum RRT value) in PI
307 and PII post-TEVAR, respectively. In PI, the highest RRT occurs at the FL proximal
308 tip in PI-2~5; while in PI-6~7, RRT is greatly decreased and the highest RRT no
309 longer occurs at the FL tip. In PII, the highest RRT also occurs at the FL proximal tip.
310 Fig.8d displays the variation of the maximum RRT (normalized by the maximum
311 RRT at the first follow-up, *i.e.* PI-2 and PII-2 for PI and PII respectively). The RRT
312 variation in PI and PII shows significant difference during short-term follow-up: the
313 normalized maximum RRT in PI increases greatly in PI-3 (from 1 to 5.516) and
314 gradually decreases afterwards to 0.00405 in PI-7; while in PII, it decreases in PII-3
315 (from 1 to 0.025) and then maintains between 0.00324-0.319. The difference in the
316 maximum RRT's variation pattern shows potential to predict different FL remodeling
317 in the two patients.

318

319 **DISCUSSION**

320 Thoracic endografts, aiming to seal the primary entry and diverting blood flow into
321 TL, are increasingly used in treating type-B aortic dissection[31]. Ideally, this
322 approach would lead to thrombosis establishment in the FL and morphologic change
323 in TL, to stabilize the aorta and consequently reduce aorta-related death. Previous
324 studies confirmed the favorable results of TEVAR; however, also reported FL
325 expansion on the segment distal to endografts, usually in the infrarenal aorta[32, 33].
326 This is related to the patency of FL[33] or, in other words, it is related to the flow field
327 and hemodynamic conditions in AoD. Current literatures provide little information
328 concerning the fate of the abdominal aorta post-TEVAR and, to our knowledge,
329 computational studies on long-term multiple follow-up cases that are able to report
330 the change of hemodynamic parameters have been lacking. Therefore, in the current
331 study, we investigate two patients showing similar physical and hemodynamic
332 features at initial presentation but presenting different FL development (stable in PI
333 and expanded in PII) during the follow-ups. We preliminarily identify the possible
334 hemodynamic parameters that could help to evaluate/predict FL enlargement and
335 thrombosis formation. In this study, the variation trends of the hemodynamic

336 parameters are more important than their absolute values.

337 The mechanical load acting on the FL boundary, which includes the outer wall of
338 FL and the flap, induces FL enlargement and at the same time restricts TL
339 remodeling. The pressure that is normally applied on the FL wall plays a key role in
340 luminal remodeling[34] and the local flow directly relates to its distribution and
341 magnitude. The flow can be assessed by its amount and the velocity. The first is
342 mainly related to the size of tears. By comparing Fig.4b~c and Table 1, it can be
343 found that the absolute flow mass passes each tear per second has positive relationship
344 with the size of the tear. This can be shown on AoT-3 of PI and AoT-2~3 of PII, since
345 they have multiple follow-up data, and it is consistent with previous report[14]. The
346 second, velocity, is determined by both the flow rate as well as the tear size; a smaller
347 tear size is correspondent to smaller flow rate yet accelerates the flow at the same
348 time. For instance, in the final two examinations of PI (PI-6 and PI-7), the amount of
349 the blood entering FL via AoT-3 decreases from 5.43% to 3.09% of the total flow and
350 the tear size decreases from 93.49mm² to 44.09mm². However, the flow passing this
351 tear has been accelerated and induces stronger impact on the FL outer wall (Fig.5e). If
352 studying a longer period (PI-4~7), the variation of W_{FL} at L3 (Fig.2e), where just
353 below AoT-3 in PI, is similar to the variation of the ratio between the diverted flow
354 amount and the tear size.

355 Along the aorta, the pressure in TL decreases generally but that in FL, due to the
356 vortical flow and its higher energy exchange, it does not present significant spatial
357 difference. The AoTs, functioning as the bridge between TL and FL, transport blood
358 flow and also pressure gradient. This induces similar pressure in the TL and FL near
359 the tears. Because of the relatively uniform P_{FL} and its connection with P_{TL} at the
360 tears, in general, P_{FL} is smaller than P_{TL} in the proximal region (above the AoTs) and
361 higher than P_{TL} in the downstream. This general distribution feature is shown in Fig.5
362 in all of the post-interventional cases at the moment of systolic peak and similar
363 patterns can be found in other time steps of the cardiac cycle.

364 At the flap, P_{FL} and P_{TL} conflict each other; the difference between them (PDiff)
365 may be associated with subsequent luminal remodeling[14]. Luminal remodeling is a
366 long-term effect; investigation of PDiff in short-term follow-ups may show the
367 variation trends of lumen remodeling, while PDiff in long-term follow-ups may be
368 consistent to lumen remodeling results. Indeed, taking L3 as an example, in short-term
369 (PI-2~3, PII-2~3), PD in PII increases from 1.44 to 2.93mmHg (7days-1month);

370 while, PDiff in PI remains about 0.55mmHg (7days-4month). This, earlier than
371 luminal change (Fig.2), shows the potential of FL enlargement for PII. In long-term
372 follow-ups (PI-4~7, PII-4~5), AoT-3 becomes the main FL flow entry in PI and
373 AoT-2 is the main entry in PII. PDiff increases from negative to positive slightly
374 below the position of AoT-3 in PI and AoT-2 in PII. Moreover, in both patients, in the
375 final examination, the maximum PDiff occurs near L3, where W_{FL} increases the most
376 (among the compared four positions) and W_{TL} in PII decreases. The abovementioned
377 indicates: (i) in short-term follow-ups, great increase of PDiff may imply potential FL
378 expansion; (ii) while, in long-term follow-up, the position of the first flow entry of FL
379 is the negative-to-positive watershed of PDiff, the position of the maximum PDiff is
380 consistent with the greatest W_{FL} increase, and when the maximum PDiff is small
381 (0.22mmHg in PI-7), the pressure induces slight FL expansion without restricted acts
382 on TL, but when it is relatively large (1.39mmHg in PII-5), both FL expansion and TL
383 collapse are found. In clinical examinations, monitoring PDiff at early-stage and
384 identifying the position of FL entries and the position of largest PDiff may assist in
385 wisely control of the untreated aorta segment.

386 The WSS is related to the formation of thrombosis. Previous studies suggested that
387 the tearing of the aortic wall and high WSS in the near region of the tears could
388 promote initial activation of platelets as well as the formation of platelet aggregates;
389 while, the highly vortical flow pattern in the FL corresponding with low WSS
390 promotes platelet aggregation and deposition, so that leads to surface thrombosis [35,
391 36]. In other words, lower WSS may induce surface thrombus and thus lead to
392 constructive FL remodeling [37, 38]. In the long-term follow-ups (PI-4~5 and
393 PII-4~5), complete thrombosis is found at the proximal region of dissection and
394 partial thrombosis remains above the re-entries. The partial thrombosis in both PI and
395 PII is aligned with the intimal flap; thus, WSS on the flap along the TL and FL sides
396 are compared. The WSS_{FL} is significantly lower than WSS_{TL} throughout the cardiac
397 cycle; the low WSS_{FL} possibly induces surface thrombus along the flap in FL while
398 the high WSS_{TL} can keep the TL patent. The lowest WSS_{FL} (<0.25Pa) occurs at the
399 proximal region of FL (Fig.7d), implying potential thrombosis in these regions.
400 Indeed, partial thrombosis in PI-4~5 with very low WSS_{FL} turns to complete
401 thrombosis in PI-6~7 (indicated by arrow in Fig.7d). Moreover, in PII, the WSS_{FL} at
402 the tip of the flap in PII-3 is small (<0.25Pa). In its next follow-up (PII-4), growth of
403 partial thrombosis can be found (indicated by arrow in Fig.7d). However, slightly

404 higher WSS_{FL} is shown in PII-4 at the proximal tip, and in its next follow-up (PII-5),
405 the partial thrombosis is slightly reduced (indicated by hollow arrow in Fig.7d). This
406 indicates the surface thrombosis is possibly very sensitive to WSS, and during the
407 long-term recovery, FL regression/growth could be repeatedly occurred at the
408 proximal tip of the FL.

409 The derived parameter of shear stress - RRT is related to particle residence and may
410 reflect thrombosis establishment as well[14]. To identify the location of high RRT,
411 Fig.8a~b draw the distribution of the normalized RRT to its maximum value in each
412 model. It shows that high RRT corresponds to the region with highly vortical and low
413 velocity flow. This occurs at the FL proximal tip for both the patients (PI-2~5,
414 PII-2~5). Moreover, Fig.8c compares the magnitude of RRT in PI-5 and PII-4, in
415 which the follow-up periods are similar (21 and 18months for PI and PII
416 respectively). The maximum RRT in PI-5 and PII-4 are 68.94 and $70.66Pa^{-1}$
417 respectively. The similar distribution pattern and magnitude of RRT in PI and PII
418 indicates that the values of RRT alone may not be able to predict FL remodeling. To
419 further investigate this, the variation of the maximum RRT is studied (Fig.8d). The
420 maximum RRTs in PI-3~7 and PII-3~5 are normalized to the correspondent first
421 follow-up results (PI-2 and PII-2, 7days post-TEVAR). The variation patterns of this
422 normalized maximum RRT show significant difference between PI and PII. This
423 implicates that, post-TEVAR, variation of RRT in short- to middle-term follow-up
424 (PI-2~5, PII-2~4) may play a key role in thrombosis establishment: an increase of
425 RRT after TEVAR and maintaining the relative normalized maximum RRT value to
426 be above 1.0 (Fig.8d) may lead to positive FL remodeling.

427 Common morphological predictors for re-intervention or surgery after TEVAR
428 include aortic diameter $>55mm$ and growth rate $>10mm/year$ [39]. Hemodynamic
429 condition of the dissected aorta plays an important role in driving TL and FL
430 remodeling. In other words, hemodynamic parameters may have the potential to
431 predict the dissection development earlier than morphological change. However,
432 hemodynamic markers that can possibly predict FL development post-TEVAR have
433 not been proposed yet, which would require long-term multiple follow-up analyses.
434 The current study investigated the correlation of hemodynamic parameters to the
435 development of post-TEVAR dissection. It preliminarily proposed the parameters that
436 are potential to differentiate the enlarged and stable FL in an early stage post-TEVAR.
437 Although this study was based on a limited number of patient cases and thus no

438 clinical conclusion can be drawn at this stage, it is the basis to future studies on a
439 larger amount of patient cases and would contribute to the research regarding early
440 decision-making on re-intervention or surgery for AoD after TEVAR.

441

442 **LIMITATIONS**

443 This study, based on long-term multiple follow-up data of two patients, preliminarily
444 shows the relationship of the variations between hemodynamic parameters and
445 luminal remodeling. However, critical values of these parameters should be better
446 determined by involving a greater number of patient cases. Besides, more detailed
447 mechanical analysis should involve the fluid-structure interaction analysis, which
448 does not only provide the stress information in the aortic wall but also offer more
449 accurate results on the WSS. However, due to the complex geometry and the lack of
450 the actual material properties, the existed fluid-structure interaction studies on AoD
451 often generate the aortic/dissection wall with arbitrary thickness and assume the
452 mechanical properties of the aortic and dissection wall similar to the properties of
453 aortic aneurysms. More accurate simulations are highly dependent on accurate model
454 establishment and material property measurements, which are currently carried on in
455 our laboratory.

456

457 **ACKNOWLEDGEMENTS**

458 This study was supported by National Natural Science Foundation of China
459 (81471752, 81353265), National Science and Technology Pillar Program of China
460 (2015BAI04B03), and National Key Research and Development Program of China
461 (2017YFC0107900). PW was partially supported by UK EPSRC (EP/N014642/1).

462

463 **CONFLICTS OF INTEREST**

464 No

465

466 **ETHICAL APPROVAL**

467 This study was approved by the Institutional Review Board of Chinese PLA General
468 Hospital (ref no. 20110903.V1.1)

469

470 REFERENCES

- 471 1. Younes, H.K., P.W. Harris, J. Bismuth, K. Charlton-Ouw, E.K. Peden, A.B. Lumsden, and M.G.
472 Davies, Thoracic endovascular aortic repair for type B aortic dissection. *Ann Vasc Surg* 2010;
473 24: p. 39-43.
- 474 2. Weber, T.F., D. Bockler, M. Muller-Eschner, M. Bischoff, M. Kronlage, H. von Tengg-Kobligk,
475 H.U. Kauczor, and A. Hyhlik-Durr, Frequency of abdominal aortic expansion after thoracic
476 endovascular repair of type B aortic dissection. *Vascular* 2016; 24: p. 567-79.
- 477 3. Doyle, B.J. and P.E. Norman, Computational Biomechanics in Thoracic Aortic Dissection:
478 Today's Approaches and Tomorrow's Opportunities. *Ann Biomed Eng* 2016; 44: p. 71-83.
- 479 4. Saad, A.A., T. Loupas, and L.G. Shapiro, Computer vision approach for ultrasound Doppler
480 angle estimation. *J Digit Imaging* 2009; 22: p. 681-88.
- 481 5. Muller-Eschner, M., F. Rengier, S. Partovi, R. Unterhinninghofen, D. Bockler, S. Ley, and H.
482 von Tengg-Kobligk, Tridirectional phase-contrast magnetic resonance velocity mapping
483 depicts severe hemodynamic alterations in a patient with aortic dissection type Stanford B. *J*
484 *Vasc Surg* 2011; 54: p. 559-62.
- 485 6. Stadlbauer, A., W. van der Riet, S. Globits, G. Crelier, and E. Salomonowitz, Accelerated
486 phase-contrast MR imaging: comparison of k-t BLAST with SENSE and Doppler ultrasound
487 for velocity and flow measurements in the aorta. *J Magn Reson Imaging* 2009; 29: p. 817-24.
- 488 7. Kohler, B., U. Preim, M. Grothoff, M. Gutberlet, K. Fischbach, and B. Preim, Motion-aware
489 stroke volume quantification in 4D PC-MRI data of the human aorta. *Int J Comput Assist*
490 *Radiol Surg* 2016; 11: p. 169-79.
- 491 8. Sakalihasan, N., C.A. Nienaber, R. Hustinx, P. Lovinfosse, M. El Hachemi, J.P. Chery-Bien,
492 L. Seidel, J.P. Lavigne, J. Quaniers, M.A. Kerstenne, A. Courtois, A. Ooms, A. Albert, J.O.
493 Defraigne, and J.B. Michel, (Tissue PET) Vascular metabolic imaging and peripheral plasma
494 biomarkers in the evolution of chronic aortic dissections. *Eur Heart J Cardiovasc Imaging* 2015;
495 16: p. 626-33.
- 496 9. Nchimi, A., J.P. Chery-Bien, T.C. Gasser, G. Namur, P. Gomez, L. Seidel, A. Albert, J.O.
497 Defraigne, N. Labropoulos, and N. Sakalihasan, Multifactorial relationship between
498 18F-fluoro-deoxy-glucose positron emission tomography signaling and biomechanical
499 properties in unruptured aortic aneurysms. *Circ Cardiovasc Imaging* 2014; 7: p. 82-91.
- 500 10. Alimohammadi, M., O. Agu, S. Balabani, and V. Diaz-Zuccarini, Development of a
501 patient-specific simulation tool to analyse aortic dissections: assessment of mixed
502 patient-specific flow and pressure boundary conditions. *Med Eng Phys* 2014; 36: p. 275-84.
- 503 11. Karmonik, C., M. Muller-Eschner, S. Partovi, P. Geisbusch, M.K. Ganten, J. Bismuth, M.G.
504 Davies, D. Bockler, M. Loebe, A.B. Lumsden, and H. von Tengg-Kobligk, Computational fluid
505 dynamics investigation of chronic aortic dissection hemodynamics versus normal aorta. *Vasc*
506 *Endovascular Surg* 2013; 47: p. 625-31.
- 507 12. Shang, E.K., D.P. Nathan, R.M. Fairman, J.E. Bavaria, R.C. Gorman, J.H. Gorman, 3rd, and
508 B.M. Jackson, Use of computational fluid dynamics studies in predicting aneurysmal
509 degeneration of acute type B aortic dissections. *J Vasc Surg* 2015; 62: p. 279-84.
- 510 13. Tse, K.M., P. Chiu, H.P. Lee, and P. Ho, Investigation of hemodynamics in the development of
511 dissecting aneurysm within patient-specific dissecting aneurysmal aortas using computational
512 fluid dynamics (CFD) simulations. *J Biomech* 2011; 44: p. 827-36.
- 513 14. Cheng, Z., N.B. Wood, R.G. Gibbs, and X.Y. Xu, Geometric and flow features of type B aortic
514 dissection: initial findings and comparison of medically treated and stented cases. *Ann Biomed*
515 *Eng* 2015; 43: p. 177-89.
- 516 15. Chen, D., M. Muller-Eschner, H. von Tengg-Kobligk, D. Barber, D. Bockler, R. Hose, and Y.
517 Ventikos, A patient-specific study of type-B aortic dissection: evaluation of true-false lumen
518 blood exchange. *Biomed Eng Online* 2013; 12: p. 65.
- 519 16. Karmonik, C., J. Bismuth, M.G. Davies, D.J. Shah, H.K. Younes, and A.B. Lumsden, A
520 computational fluid dynamics study pre- and post-stent graft placement in an acute type B
521 aortic dissection. *Vasc Endovascular Surg* 2011; 45: p. 157-64.
- 522 17. Cheng, S.W., E.S. Lam, G.S. Fung, P. Ho, A.C. Ting, and K.W. Chow, A computational fluid
523 dynamic study of stent graft remodeling after endovascular repair of thoracic aortic dissections.
524 *J Vasc Surg* 2008; 48: p. 303-9.
- 525 18. Chen, D., M. Muller-Eschner, D. Kotelis, D. Bockler, Y. Ventikos, and H. von Tengg-Kobligk,

526 A longitudinal study of Type-B aortic dissection and endovascular repair scenarios:
527 computational analyses. *Med Eng Phys* 2013; 35: p. 1321-30.

528 19. Karmonik, C., J. Bismuth, D.J. Shah, M.G. Davies, D. Purdy, and A.B. Lumsden,
529 Computational study of haemodynamic effects of entry- and exit-tear coverage in a DeBakey
530 type III aortic dissection: technical report. *Eur J Vasc Endovasc Surg* 2011; 42: p. 172-7.

531 20. Naim, W.N.W.A., P. Ganesan, Z. Sun, K. Osman, and E. Lim, The impact of the number of
532 tears in patient-specific stanford type B aortic dissecting aneurysm: CFD simulations. *J Mech
533 Med Biol* 2014; 14: p. 1450017.

534 21. Alimohammadi, M., J.M. Sherwood, M. Karimpour, O. Agu, S. Balabani, and V.
535 Diaz-Zuccarini, Aortic dissection simulation models for clinical support: fluid-structure
536 interaction vs. rigid wall models. *Biomed Eng Online* 2015; 14: p. 34.

537 22. Qiao, A., W. Yin, and B. Chu, Numerical simulation of fluid-structure interaction in bypassed
538 DeBakey III aortic dissection. *Comput Methods Biomech Biomed Engin* 2015; 18: p. 1173-80.

539 23. Clough, R.E., V.E. Zymvragoudakis, L. Biasi, and P.R. Taylor, Usefulness of new imaging
540 methods for assessment of type B aortic dissection. *Ann Cardiothorac Surg* 2014; 3: p. 314-8.

541 24. Birjiniuk, J., J.M. Ruddy, E. Iffrig, T.S. Henry, B.G. Leshnower, J.N. Oshinski, D.N. Ku, and
542 R.K. Veeraswamy, Development and testing of a silicone in vitro model of descending aortic
543 dissection. *J Surg Res* 2015; 198: p. 502-7.

544 25. Soudah, E., P. Rudenick, M. Bordone, B. Bijmens, D. Garcia-Dorado, A. Evangelista, and E.
545 Onate, Validation of numerical flow simulations against in vitro phantom measurements in
546 different type B aortic dissection scenarios. *Comput Methods Biomech Biomed Engin* 2015; 18:
547 p. 805-15.

548 26. Vignon-Clementel, I.E., C.A. Figueroa, K.E. Jansen, and C.A. Taylor, Outflow boundary
549 conditions for three-dimensional finite element modeling of blood flow and pressure in arteries.
550 *Comput Methods Biomech Biomed Engin* 2006; 195: p. 3776-96.

551 27. Ganten, M.K., T.F. Weber, H. von Tengg-Kobligk, D. Bockler, W. Stiller, P. Geisbusch, G.W.
552 Kauffmann, S. Delorme, M. Bock, and H.U. Kauczor, Motion characterization of aortic wall
553 and intimal flap by ECG-gated CT in patients with chronic B-dissection. *Eur J Radiol* 2009; 72:
554 p. 146-53.

555 28. Papaharilaou, Y., D.J. Doorly, and S.J. Sherwin, The influence of out-of-plane geometry on
556 pulsatile flow within a distal end-to-side anastomosis. *J Biomech* 2002; 35: p. 1225-39.

557 29. Bortolotto, L.A. and M.E. Safar, Blood pressure profile along the arterial tree and genetics of
558 hypertension. *Arq Bras Cardiol* 2006; 86: p. 166-9.

559 30. Gorring, N., L. Kark, A. Simmons, and T. Barber, Determining possible thrombus sites in an
560 extracorporeal device, using computational fluid dynamics-derived relative residence time.
561 *Comput Methods Biomech Biomed Engin* 2015; 18: p. 628-34.

562 31. Nienaber, C.A., S. Kische, H. Ince, and R. Fattori, Thoracic endovascular aneurysm repair for
563 complicated type B aortic dissection. *J Vasc Surg* 2011; 54: p. 1529-1533.

564 32. Andacheh, I.D., C. Donayre, F. Othman, I. Walot, G. Kopchok, and R. White, Patient outcomes
565 and thoracic aortic volume and morphologic changes following thoracic endovascular aortic
566 repair in patients with complicated chronic type B aortic dissection. *J Vasc Surg* 2012; 56: p.
567 644-50.

568 33. Sigman, M.M., O.P. Palmer, S.W. Ham, M. Cunningham, and F.A. Weaver, Aortic morphologic
569 findings after thoracic endovascular aortic repair for type B aortic dissection. *JAMA Surg* 2014;
570 149: p. 977-83.

571 34. Sueyoshi, E., I. Sakamoto, K. Hayashi, T. Yamaguchi, and T. Imada, Growth rate of aortic
572 diameter in patients with type B aortic dissection during the chronic phase. *Circulation* 2004;
573 110: p. II256-61.

574 35. Sheriff, J., D. Bluestein, G. Girdhar, and J. Jesty, High-shear stress sensitizes platelets to
575 subsequent low-shear conditions. *Ann Biomed Eng* 2010; 38: p. 1442-50.

576 36. Goel, M.S. and S.L. Diamond, Adhesion of normal erythrocytes at depressed venous shear
577 rates to activated neutrophils, activated platelets, and fibrin polymerized from plasma. *Blood*
578 2002; 100: p. 3797-803.

579 37. Wu, M.H., Y. Kouchi, Y. Onuki, Q. Shi, H. Yoshida, S. Kaplan, R.F. Viggers, R. Ghali, and L.R.
580 Sauvage, Effect of differential shear stress on platelet aggregation, surface thrombosis, and
581 endothelialization of bilateral carotid-femoral grafts in the dog. *J Vasc Surg* 1995; 22: p.
582 382-90.

- 583 38. Menichini, C., Z. Cheng, R.G. Gibbs, and X.Y. Xu, Predicting false lumen thrombosis in
584 patient-specific models of aortic dissection. *J R Soc Interface* 2016; 13: p. 20160759.
- 585 39. Erbel, R., V. Aboyans, C. Boileau, E. Bossone, R.D. Bartolomeo, H. Eggebrecht, A.
586 Evangelista, V. Falk, H. Frank, O. Gaemperli, M. Grabenwoger, A. Haverich, B. Iung, A.J.
587 Manolis, F. Meijboom, C.A. Nienaber, M. Roffi, H. Rousseau, U. Sechtem, P.A. Sirnes, R.S.
588 Allmen, and C.J. Vrints, 2014 ESC Guidelines on the diagnosis and treatment of aortic diseases:
589 Document covering acute and chronic aortic diseases of the thoracic and abdominal aorta of
590 the adult. The Task Force for the Diagnosis and Treatment of Aortic Diseases of the European
591 Society of Cardiology (ESC). *Eur Heart J* 2014; 35: p. 2873-926.
- 592

FIGURE LEGENDS

- Fig.1** (a)~(d) display the reconstructed models of AoD (D-days, M-months); (e) is a sonogram of Doppler ultrasound velocimetry, the upper edge of which is shown in green; (f) shows an axial slice of CTA scan at initial presentation of PI, in which the segmented lumen boundary is shown in yellow.
- Fig.2** The luminal remodeling. (a) displays the measured axial positions (L1-4) and the regions to calculate luminal volume (V_{TL} , V_{TL} -Part and V_{FL}); (b)~(e) show the variation of luminal volume, aortic diameter, width of TL and FL respectively.
- Fig.3** Flow patterns of AoD. (a)~(b) display the flow streamlines at systolic peak; (c) shows the streamlines at the proximal region of FL in the final model of PII.
- Fig.4** Flow exchange between the true and false lumen. (a) displays the variation of the mass flow rate towards the FL via the primary entry, AoT-2 and AoT-3 over a cardiac cycle at initial presentation; (b) and (c) respectively show the mass flow rate variation at AoT-2 and AoT-3 during the longitudinal follow-ups.
- Fig.5** Pressure distribution along the dissected aorta. (a) and (b) display the PDsys distribution in PI and PII respectively; (c) shows the PDsys in a normal aorta; (d) displays the variation of the maximum PDsys during the follow-up; (e) shows the Psys at a slice crossing the FL in the final two examinations of PI and in the final examination of PII; and (f) shows the region with $P_{sys} \geq 99.15$ mmHg (in red).
- Fig.6** Pressure difference between FL and TL for PI (a)~(d) and PII (e)~(f).
- Fig.7** WSS distribution along the flap. (a) and (b) display the WSS distribution at systolic peak on the flap of TL and FL side respectively; (c) and (d) show the WSS distribution on the flap of FL side during the long-term follow-ups in different WSS ranges.
- Fig.8** RRT distribution and variation. (a) and (b) show the normalized RRT to its maximum value post-TEVAR in PI and PII respectively; (c) shows the RRT distribution at PI-5 and PII-4, where the follow-up periods in PI and PII are similar; and (d) displays the variation of the normalized maximum RRT to its value in the first follow-up (PI-2 for PI and PII-2 for PII).

Hemodynamic Parameters That May Predict False-lumen Growth in Type-B Aortic Dissection after Endovascular Repair: A Preliminary Study on Long-term Multiple Follow-ups

Huanming Xu^{1,2}, Zhenfeng Li^{1,2}, Huiwu Dong³, Yilun Zhang¹, Jianyong Wei¹, Paul N. Watton^{5,6}, Wei Guo⁷, Duanduan Chen^{1,2*}, Jiang Xiong^{7*}

¹School of Life Science, Beijing Institute of Technology, China

²Key Laboratory of Convergence Medical Engineering System and Healthcare Technology, The Ministry of Industry and Information Technology, Beijing Institute of Technology, China

³Department of Ultrasound Diagnosis, Chinese PLA General Hospital, China

⁵Department of Computer Science & INSIGNEO Institute, University of Sheffield, UK

⁶Department of Mechanical Engineering and Material Science, University of Pittsburgh

⁷Department of Vascular and Endovascular Surgery, Chinese PLA General Hospital, China

***Corresponding author:** Prof Duanduan Chen

School of Life Science, Beijing Institute of Technology, Beijing,
100081, China.

Tel. +86-10-68912154

Email. duanduan@bit.edu.cn

Dr Jiang Xiong

Department of Vascular and Endovascular Surgery,
Chinese PLA General Hospital, Beijing, 100853, China.

Tel. +86-10-66938349

Email. xiongjiangdoc@126.com

1 **ABSTRACT**

2 Thoracic endovascular aortic repair (TEVAR) is commonly applied in type-B aortic
3 dissection. For patients with dissection affects descending aorta and extends downward to
4 involve abdominal aorta and possibly iliac arteries, false lumen (FL) expansion might occur
5 post-TEVAR. Predictions of dissection development may assist in medical decision on
6 re-intervention or surgery. In this study, two patients are selected with similar morphological
7 features at initial presentation but with different long-term FL development post-TEVAR
8 (stable and enlarged FL). Patient-specific models are established for each of the follow-ups.
9 Flow boundaries and computational validations are obtained from Doppler ultrasound
10 velocimetry. By analyzing the hemodynamic parameters, the false-to-true luminal pressure
11 difference (PDiff) and particle relative residence time (RRT) are found related to FL
12 remodeling. It is found that (i) the position of the first FL flow entry is the watershed of
13 negative-and-positive PDiff and, in long-term follow-ups, and the position of largest PDiff is
14 consistent with that of the greatest increase of FL width; (ii) high RRT occurs at the FL
15 proximal tip and similar magnitude of RRT is found in both stable and enlarged cases; (iii)
16 comparing to the RRT at 7days post-TEVAR, an increase of RRT afterwards in short-term is
17 found in the stable case while a slight decrease of this parameter is found in the enlarged case,
18 indicating that the variation of RRT in short-term post-TEVAR might be potential to predict
19 long-term FL remodeling.

20

21 **Key Words:** aortic dissection; hemodynamics; endovascular procedures.

22 INTRODUCTION

23 Aortic dissection (AoD) is a severe cardiovascular disease, where a surge of blood
24 flowing into the aortic wall via an initial tear or damage of the intima and splitting the
25 single aortic lumen into a true and false lumen (TL and FL). Stanford type-B AoD
26 indicates those with the dissection begins distal to the supraaortic branches.
27 Interventional treatment of Stanford type-B AoD commonly involves thoracic
28 endovascular aortic repair (TEVAR)[1]. In a number of patients, FL expansion is
29 found post-TEVAR, especially in the infrarenal aorta. Recent study confirmed that
30 abdominal aortic expansion can be frequently found after TEVAR and is independent
31 from thoracic FL thrombosis[2]. Prediction of FL growth may contribute to early
32 decision-making of re-intervention or surgery. The post-TEVAR development of
33 dissection is highly dependent on local hemodynamics[3]. Medical imaging tools such
34 as Doppler ultrasound[4] and phase-contrast MR (pcMR)[5] are able to capture the
35 flow velocity within aorta. However, the former provides velocity information at a
36 certain position of the vessel, and the latter reveals flow movement with relatively low
37 spatial and temporal resolution[6, 7]. On the other hand, the uptake of
38 ^{18}F -fluorodeoxyglucose in PET-CT can indicate complications in AoD[8] and positive
39 correlation between the uptake and wall shear stress is found in aortic aneurysm
40 study[9]; however, PET-CT is relatively expensive and the flow information cannot be
41 directly reported. Thus, computational simulations that can provide hemodynamic
42 parameters, such as flow, pressure and shear stress distributions, may enrich analysis.

43 Previous computational works focusing on type-B AoD include investigations on
44 hemodynamic features[10-14], luminal flow exchange[12, 15], post-TEVAR flow
45 effects[16-18], tear-induced flow effects[19, 20] and fluid-structure interaction
46 studies[21, 22]. Besides, 4D pcMR[5, 23] and phantom[24, 25] measurements have been
47 conducted to compare with or validate the computed results. In this study, we
48 investigate the flow-driven dissection development after TEVAR based on long-term
49 multiple follow-ups. Flow conditions in patients with stable and enlarged FL are
50 compared and key hemodynamic parameters that are related to dissection growth in
51 abdominal aorta are proposed, facilitating medical decision-making on post-TEVAR
52 treatment.

53

54

55 **METHODS**

56 *Image Acquisition and Model Reconstruction*

57 This study was approved by the institutional review board of the Chinese PLA
58 General Hospital. Written informed consent was obtained from the patients involved
59 in this study. Two male patients (PI and PII) with subacute Stanford type-B AoD
60 underwent arterial-phase CT angiography (CTA) at initial presentation and during the
61 follow-up examinations after TEVAR via a dual-source CT scanner (SOMATOM
62 Definition Flash, SIEMENS, Germany). Details of the CTA scan and the patient
63 information are described in S1, Supporting Document. Image segmentation and
64 surface reconstruction of AoD were conducted through Mimics (Materialise,
65 Belgium). The cross-sectional contours of the reconstructed geometries were mapped
66 back to CTA images to ensure that the 3D models present the actual outline of the
67 vessel lumen. Detailed views of the models are shown in Fig.1, where PI/II-1
68 indicates the models pre-TEVAR while PI/II-2 and others are models post-TEVAR.
69 After TEVAR, PI and PII have experienced six- (7days~53months) and four-times
70 (7days~35months) CTA scans. The FL in PI was in stable condition (PI-2~7, Fig.1b)
71 while that in PII was expanding (PII-2~5, Fig.1d). The models were meshed in ICEM
72 (ANSYS Inc, Canonsburg, USA) with tetrahedral elements in the core region and
73 prismatic cells (10 layers) in the boundary layer near the aortic wall. The grid
74 resolution varies from 2,564,019 to 3,153,829 cells.

75

76 *Doppler Ultrasound and Boundary Conditions*

77 Time-variant velocities at ascending aorta (AAo), brachiocephalic trunk (BT), left
78 common carotid artery (LCCA), left subclavian artery (LSA) were measured via
79 Doppler ultrasound of the patients, and velocity variation at the distal thoracic aorta
80 (DTAo, about 5cm above celiac trunk) was measured in the final examination of PI to
81 provide validation of the computational results. This is because the true lumen (TL)
82 remodeling at this position in PI is sufficient, so that relatively organized flow is
83 found and the central line of vessel can be accurately identified. The velocity of AAo
84 was measured through the apical 5-chamber view and the suprasternal long axis view
85 of aortic arch. The two results were compared to ensure the maximum velocity at
86 AAo could be captured. For other arteries (BT, LCCA, LSA and DTAo), Doppler

87 velocimetry has been conducted at the proximal and distal sites of the targeted
88 measurement vessel. Mean velocity over a cardiac cycle at the two sites for each
89 particular vessel was then calculated and compared. When the difference between
90 them is less than 5%, the measured velocity is considered effective. Details of the
91 measurement are described in S2, Supporting Document.

92 The upper edge of the velocity sonogram was extracted (Fig.1e) as the variation of
93 the maximum velocity at the measured site. The flow rates at AAo, BT, LCCA and
94 LSA, as the velocity boundary conditions, can then be calculated based on the
95 measured time-variant maximum velocity and the assumed flat flow profile for AAo
96 and parabolic flow profile for the others. The velocity boundary conditions of the
97 models is shown in Fig.S1a, Supporting Document. Pulsatile waveforms of the
98 pressure at celiac artery (CA), superiormesenteric artery (SMA), renal arteries and the
99 outlets at common iliac arteries were obtained from previous study[26] (Fig.S1b,
100 Supporting Document). As shown in Fig.1, two models in PII (PII-1 and PII-4) were
101 cropped below the iliac bifurcation due to the relatively shorter CT scanning range. To
102 eliminate the outlet effects, time-variant pressure distribution at the cropping plane
103 has been calculated in PII-2~3 and PII-5. The averaged pressure information at this
104 cropping plane was mapped to PII-1 and PII-4, serving as the pulsatile pressure
105 outlets.

106

107 *Numerical Models*

108 The vessel wall was assumed as no-slip and rigid, due to low distensibility in
109 long-term follow-ups[27]. **The blood was treated as Newtonian and incompressible**
110 **with density of 1044kg/m^3 and dynamic viscosity of $0.00365\text{kg}\cdot\text{m}^{-1}\cdot\text{s}^{-1}$ [28].** The
111 average Reynolds number over a cardiac cycle, calculated based on the equivalent
112 diameter ($D_e = 2\sqrt{\text{Area}/\pi}$) and velocity at the inlet of the ascending aorta in PI and
113 PII, were between 2066-2197 and 2844-2960, respectively. Our previous study
114 confirmed that laminar simulations with adequately fine mesh resolutions, especially
115 refined near the walls, can capture flow patterns as turbulence model[15]. To further
116 confirm this, we solved the flow in the first follow-up cases (PI-2 and PII-2) by both
117 laminar and k- ω SST turbulence models, where the flow in the abdominal aortic
118 region is the fastest during the follow-ups. Similar flow patterns were found and the
119 discrepancy of the maximum velocity and wall shear stress (WSS) in the abdominal

120 aorta was 4.2% and 5.2% respectively (the laminar and turbulent results of PII-2 were
121 shown in Fig.S2, Supporting Document), ensuring the rationality of laminar model to
122 be applied in the current problem. A finite volume solver, CFD-ACE+ (ESI Group,
123 France) was employed. The heart-beat cycle of the patients was measured at each
124 clinical examination. The averaged cardiac cycle for PI and PII were 71 and
125 69beat/min respectively. Temporal discretization of numerical models was assigned as
126 45step/cycle. Simulation was carried out for 5 cardiac cycles to achieve a periodic
127 solution and results of the final cycle were presented. Grid and temporal
128 independency analyses on finer grids and finer temporal discretizations were
129 conducted to ensure the base resolution with the base time step settings are adequate
130 (S3, Supporting Document).

131

132 **RESULTS**

133 *Aortic Remodeling*

134 Aortic remodeling was assessed by: (i) size and numbers of the aortic tears (AoT), (ii)
135 change of luminal volume, and (iii) growth of aortic diameter. There are four major
136 AoTs along the aorta for both patients at initial presentation. The primary entry
137 (AoT-1) in both patients is located at the proximal region of descending aorta and the
138 locations of other AoTs (AoT-2~4) are displayed in Fig.1. After TEVAR, the primary
139 entry was sealed and after the first follow-up of PI, AoT-2 was disappeared.
140 Considering the position and local aortic curvature of the tears, AoT-4 is the exit of
141 the flow from FL to TL, while the function of AoT-2 and AoT-3 is uncertain. Since
142 only the flow entries towards the FL is able to bring mechanical impact into the
143 dissection, size measurement was only performed on AoT-2 and AoT-3 (Table 1).
144 Post-TEVAR, both AoT-2 and AoT-3 in PI and PII are enlarged, probably due to the
145 greater flow impact on these sites after AoT-1 was sealed.

Table 1. The size of the aortic tears in the patients with long-term follow-ups

Tear	Geometry	PI-1	PI-2	PI-3	PI-4	PI-5	PI-6	PI-7
AoT-2	H[mm]	7.87	7.15	-	-	-	-	-
	W[mm]	8.97	10.76	-	-	-	-	-
	A[mm ²]	64.61	70.71	-	-	-	-	-
AoT-3	H[mm]	13.86	18.79	17.93	15.31	18.23	8.81	8.57
	W[mm]	10.04	9.38	6.03	8.90	7.30	6.72	5.75
	A[mm ²]	116.13	150.82	106.40	119.19	128.82	93.49	44.09
Tear	Geometry	PII-1	PII-2	PII-3	PII-4	PII-5		
AoT-2	H[mm]	8.17	8.41	5.74	11.04	11.20		
	W[mm]	9.34	9.96	7.36	9.59	6.03		
	A[mm ²]	62.61	70.47	37.33	89.50	54.05		
AoT-3	H[mm]	9.91	9.55	7.77	6.25	6.19		
	W[mm]	10.01	11.47	9.34	8.04	9.90		
	A[mm ²]	85.27	99.32	61.51	40.35	53.32		

H-Height; W-Width; A-Area.

146

147 The change of luminal volume is shown in Fig.2. The volume of TL (V_{TL}) involves
148 the initial dissection-affected TL region, while $V_{TL-Part}$ indicates the
149 dissection-affected TL region during the follow-ups. Variations of V_{TL} , volume of FL
150 (V_{FL}) and the ratio between $V_{TL-Part}$ and V_{FL} are displayed in Fig.2b. V_{FL} in the stable
151 case (PI) reduces gradually post-TEVAR, except for the final examination, where a
152 trivial increase of V_{FL} is found (131.6mm³ in 20months). However, V_{FL} in the
153 expanding case (PII) reduces in the first two follow-ups but enlarges afterwards,
154 where the V_{FL} growths in PII-4 and PII-5 are 2,138mm³ and 34,989mm³ respectively,
155 the durations of which are both 17months (Fig.2b). For both cases, the TL-to-FL
156 volume ratio ($V_{TL-Part}/V_{FL}$) keeps increasing, except for PI-6 and PII-3 (pointed by
157 arrows). This is because significant FL regression occurs at the proximal region (blue
158 squares in Fig.1b,1d), which shortens the comparison region. Since TL remodeling is
159 insufficient in this region, value of $V_{TL-Part}/V_{FL}$ reduces. The averaged increase rates of
160 $V_{TL-Part}/V_{FL}$ in the follow-ups of PI and PII are 1.8% and 0.3% per month,
161 respectively, indicating a significant luminal remodeling difference.

162 The aortic diameter (D) is measured in each model, taking into account the width of
163 TL and FL (W_{TL} and W_{FL}) and the thickness of flap. As shown in Fig.1f,
164 measurements have been conducted in the axial plane of the CTA datasets, along a
165 line that crosses the centre of the flap and is perpendicular to the flap. Four
166 measurement positions are selected in the abdominal aorta. As shown in Fig.2a, they
167 are 1cm below diaphragm (L1), 1cm above CA (L2), 3.5cm below SMA (L3) and 9cm
168 below SMA (L4). Fig.2c~e display the variation of D, W_{TL} and W_{FL} respectively.
169 Positive TL remodeling is found in PI and PII in general, except for L3 and L4 in PI-3

170 and L3 in PII-4~5. W_{FL} at the proximal region of PI (L1 and L2) reduces greatly
171 during the follow-up, while in the distal region (L3 and L4), variation of W_{FL} is stable.
172 In PII, W_{FL} increases sharply since the second follow-up (PII-3). Comparing the
173 variation of W_{TL} , W_{FL} and D , it can be found that the variation pattern of D is mainly
174 determined by the variation of W_{FL} .

175

176 *Flow Pattern, Validation and Luminal Flow Exchange*

177 Fig.3 shows the flow streamlines at systolic peak where the color map of velocity
178 magnitude is restricted to a certain range in PI (0~2.51m/s) and PII (0~3.78m/s) to
179 assist visualization of the longitudinal velocity variation. At systolic peak, fast and
180 organized flow is found in TL; while vortical and relatively slow flow presents in FL.
181 Highest velocity presents in the short-term follow-ups (PI-2~3, 4months for PI;
182 PII-2~3, 1months for PII) at the region below stentgraft and above AoT-2 and -3,
183 where TL remodeling is insufficient and the blood has not been diverted. In long-term
184 follow-ups (PI-4~7 and PII-4~5), the flow in the proximal FL is generally slow
185 (<0.5mm/s); while below AoT-2 (the first re-entry), where blood perfusion occurs,
186 faster flow up to 1.53m/s in PI and 2.22m/s in PII are found in the FL with helical
187 feature (Fig.3c).

188 To validate the computational results, Doppler ultrasound velocimetry was
189 performed at distal thoracic aorta (5cm above CA) along the centerline of TL. This
190 was only conducted at the final examination of PI, because its TL in the distal thoracic
191 aorta is fully remodeled and the local flow is therefore organized (Fig.3a). The
192 measured and computed velocities at the centre of the cross-section of the vessel, 5cm
193 above CA, are 1.58m/s and 1.66m/s respectively, indicating a difference of 5.1%.
194 Moreover, the computed velocity variation pattern is similar to the measured one
195 (Fig.S3, Supporting Document), ensuring the rationality of computational results.

196 Fig.4 displays the luminal flow exchange via the primary entry for initial
197 presentation and that via AoT-2 and AoT-3 during the follow-ups. As
198 abovementioned, AoT-4 functions as the outlet of FL throughout the cardiac cycle,
199 thus it is not displayed in Fig.4. As shown in Fig.4a (positive values indicates flow
200 enters FL), before treatment, the TL-to-FL flow exchange in PI and PII presents
201 similar pattern: the primary entry serves as the main flow inlet of FL; AoT-2 functions
202 as the outlet of FL in the initial part of systole and behaves as inlet in the rest part of

203 cardiac cycle; and AoT-3 mainly serves as the outlet of FL. There are 31.48% and
204 40.00% of the total flow diverted to FL over a cardiac cycle for PI and PII
205 respectively, at initial presentation. After TEVAR, the function of the tears changes. In
206 PI, AoT-2 becomes the inlet of FL in the entire heart-beat cycle (Fig.4b), while AoT-3
207 functions as the inlet of FL during systole and serves as the outlet in diastole (Fig.4c).
208 Since the second follow-up of PI, AoT-2 is closed and AoT-3 gradually becomes the
209 inlet of FL throughout the entire cardiac cycle. The flow entering FL are 16.67%,
210 6.98%, 8.24%, 9.59%, 5.43%, 3.09% of the total flow for case PI-2~7 respectively,
211 the variation of which is consistent to the variation of tear size (Table 1) and it is
212 generally reducing. In PII, both of AoT-2 and AoT-3 are existed during the follow-ups.
213 AoT-2 mainly serves as the inlet of FL; especially in model PII-4 and PII-5, positive
214 values of mass flow rate are found in the entire cardiac cycle (Fig.4b). AoT-3 diverts a
215 small amount of flow into the FL during systole and mainly behaves as the outlet of
216 FL (Fig.4c). There are 5.22%, 3.06%, 14.76% and 10.23% of the total flow diverted
217 into FL in case PII-2~5 respectively, the variation of which is also consistent with the
218 variation of tear size.

219

220 *Loading Distribution along the Aorta*

221 Fig.5a~b display the pressure drop at systolic peak (PD_{sys}, the difference between the
222 local pressure and the pressure at the bottom of the model). In TL, PD_{sys} reduces
223 from the inlet of AAo to the outlets of common iliac arteries. At initial presentation
224 (PI-1 and PII-1), FL diverts part of the total flow (31.48% for PI and 40.00% for PII),
225 maintaining PD_{sys} in relatively low values. After TEVAR, in short-term follow-ups
226 (PI-2~3 and PII-2~3), proximal descending aorta is supported by stentgraft and
227 reshaped; however, below the endograft, TL remains collapsed, inducing larger
228 resistance and resulting in higher velocity and regional lower pressure in this region
229 (indicated by arrows in Fig.5a~b). In long-term follow-ups (PI-4~7 and PII-4~5), TL
230 remodeling in distal thoracic aorta is improved; PD_{sys} thus gradually reduces along
231 aorta. In contrary, PD_{sys} in FL is relatively uniform, which is probably due to the
232 higher energy exchange induced by the vortical flow. Fig.5d shows the variation of
233 the maximum PD_{sys} during the follow-ups. For both patients, the maximum PD_{sys}
234 increases greatly soon after TEVAR (7days); along with the progress of TL
235 remodeling, the maximum PD_{sys} reduces. The PD_{sys} in normal aorta model (Fig.5c)

236 based on the same boundary conditions as PI and PII is also computed and the
237 averaged maximum PDsys is shown by the dash line in Fig.5d. Since the growth of
238 FL in the two patients shows obvious difference, the similar variation pattern of
239 PDsys indicates that the pressure drop is mainly affected by TL remodeling.

240 The mean arterial pressure drop (PDmean) from AAO to the common iliac arteries
241 during a cardiac cycle is also calculated. It is 6.29mmHg for the initial model of PI
242 and 4.70mmHg for the final model (53months post-TEVAR), which is slightly higher
243 than that in normal aorta for the studied segment (4mmHg[29]). The PDmean of PII at
244 the initial and final (35months post-TEVAR) models are 6.53mmHg and 6.07mmHg,
245 respectively, consistent with its insufficient TL remodeling.

246 In the final examination of PI (PI-7), V_{FL} is slightly increased, D and W_{FL} also
247 increase at L3 (Fig.2); however, the flow exchange and tear size at this stage are both
248 reduced. Fig.5e displays the pressure distribution at systolic peak (P_{sys}) on a slice of
249 FL for PI-6~7. It shows that the smaller tear size reduces the flow entering FL,
250 however, it increases the velocity and induces higher pressure impact on the outer
251 wall of FL (indicated by arrows in Fig.5e). The highest pressure of the impact region
252 in PI and PII at final examination are 114.37 and 115.41mmHg respectively. Besides,
253 by blanking the region with $P_{sys} < 109.15$ mmHg, which is the 95% of the averaged
254 maximum pressure in PI and PII at final examination, Fig.5f shows that the high
255 pressure region (in red) in the FL of PII is much larger than that in PI. In fact, the FL
256 growth rates of PI and PII at the final examination are $0.22\text{mm}^3/\text{day}$ and
257 $68.61\text{mm}^3/\text{day}$ respectively.

258

259 *Luminal Pressure Difference, Wall Shear Stress and Relative Residence Time*

260 To investigate the pressure difference (PDiff) between TL and FL, a series of slices
261 that are perpendicular to the centerline of TL are extracted and the net pressures in TL
262 (P_{TL}) and FL (P_{FL}) on each slice over a cardiac cycle are calculated. Fig.6 displays
263 PDiff ($\text{PDiff} = P_{FL} - P_{TL}$) in each model. In both patients, pre-TEVAR (Fig.6a,6e), P_{FL} is
264 smaller than P_{TL} at the level above AoT-2; while, below AoT-2, P_{FL} is larger than P_{TL} ,
265 pushing the FL towards TL. Post- TEVAR, the primary entry is closed. In PI, negative
266 values of PDiff are found above AoT-3 (Fig.6b~c), indicating higher P_{TL} presents in
267 this region, which supports the aortic wall and assists in TL expansion. However, in
268 the region below AoT-3 in PI, due to the blood perfusion into the FL, positive values

269 of PDiff present, indicating FL propulsion on the TL. In the final follow-up of PI
270 (Fig.6d), the maximum value of PDiff is 0.22mmHg. This maximum PDiff occurs
271 close to L3. At this position, W_{FL} and W_{TL} increase by 1.02mm and 0.46mm
272 respectively (Fig.2), indicating this small value of PDiff (0.22mmHg) is not large
273 enough to squeeze TL but the local pressure in FL (Fig.5e) is able to induce further
274 FL expansion. On the other hand, in PII, post-TEVAR, AoT-2 becomes the main inlet
275 of the flow into FL. Higher above this tear, P_{TL} is larger than P_{FL} , supporting TL
276 expansion (Fig.6e~f). In the near region above AoT-2, TL remodeling is insufficient
277 for the short-term follow-ups but P_{FL} gradually increases; thus, regional positive PDiff
278 is found in PII-3 above AoT-2 (arrow indicated in Fig.6f). Below AoT-2, positive
279 values of PDiff dominate and the maximum PDiff in the final examination of PII is
280 1.39mmHg, more than 6-times as high as that in PI, occurring close to L3. Taking
281 account of that, in PII-5, W_{TL} decreases yet W_{FL} increases at L3 (Fig.2d~e), this high
282 PDiff propels TL collapse and the local pressure pushes FL growth.

283 Fig.7 shows the wall shear stress (WSS) distribution on the flap at systolic peak. Its
284 variation over a cardiac cycle is shown in Video S1-6, Supporting Document. In both
285 patients, the WSS on the flap at the FL side (WSS_{FL}) is significantly smaller than that
286 on the TL side (WSS_{TL}); and the WSS_{TL} in PII is generally higher than that in PI. At
287 initial presentation, the maximum WSS_{TL} occurs at the edge of primary entry; while
288 the maximum WSS_{FL} occurs at the proximal descending aorta along the side opposite
289 to the primary entry (indicated by arrows in Fig.7b). In follow-ups, the maximum
290 WSS_{TL} occurs at the region where TL presents most collapse; while the maximum
291 WSS_{FL} occurs at the edge of the tears. AoT-3 and AoT-2 are the main FL flow entries
292 for PI and PII in follow-ups, which induces helical flow in the downstream and high
293 WSS_{FL} on the side opposite to the tears (indicated by hollow arrows in Fig.7b). To
294 further visualize the variation of WSS_{FL} at different regions along the flap on the FL
295 side, the color map is assigned to 0~5Pa (Fig.7c) and 0~0.5Pa (Fig.7d) to show the
296 distal and proximal region respectively. In PI, WSS_{FL} at the region below AoT-3
297 reduces obviously from PI-4 to PI-6; however, in the final examination, it is slightly
298 increased, although the maximum WSS_{FL} in this region is still smaller than 1Pa. In
299 PII, WSS_{FL} presents obvious increase in PII-4 and reduces slightly in PII-5; the
300 maximum WSS_{FL} at the region between AoT-2 and AoT-3 in the final examination is
301 5.21Pa.

302 Particle residence time is proposed to be related to thrombosis establishment[14].

303 The relative residence time (RRT), which is based on the time-averaged WSS
304 (TAWSS) and oscillatory shear index (OSI), $[(1-2 \cdot \text{OSI}) \cdot \text{TAWSS}]^{-1}$, reflects particle
305 residence time and thus may correspond with the region of thrombosis[14, 30].
306 Fig.8a~b show the RRT distributions (normalized by the maximum RRT value) in PI
307 and PII post-TEVAR, respectively. In PI, the highest RRT occurs at the FL proximal
308 tip in PI-2~5; while in PI-6~7, RRT is greatly decreased and the highest RRT no
309 longer occurs at the FL tip. In PII, the highest RRT also occurs at the FL proximal tip.
310 Fig.8d displays the variation of the maximum RRT (normalized by the maximum
311 RRT at the first follow-up, *i.e.* PI-2 and PII-2 for PI and PII respectively). The RRT
312 variation in PI and PII shows significant difference during short-term follow-up: the
313 normalized maximum RRT in PI increases greatly in PI-3 (from 1 to 5.516) and
314 gradually decreases afterwards to 0.00405 in PI-7; while in PII, it decreases in PII-3
315 (from 1 to 0.025) and then maintains between 0.00324-0.319. The difference in the
316 maximum RRT's variation pattern shows potential to predict different FL remodeling
317 in the two patients.

318

319 **DISCUSSION**

320 Thoracic endografts, aiming to seal the primary entry and diverting blood flow into
321 TL, are increasingly used in treating type-B aortic dissection[31]. Ideally, this
322 approach would lead to thrombosis establishment in the FL and morphologic change
323 in TL, to stabilize the aorta and consequently reduce aorta-related death. Previous
324 studies confirmed the favorable results of TEVAR; however, also reported FL
325 expansion on the segment distal to endografts, usually in the infrarenal aorta[32, 33].
326 This is related to the patency of FL[33] or, in other words, it is related to the flow field
327 and hemodynamic conditions in AoD. Current literatures provide little information
328 concerning the fate of the abdominal aorta post-TEVAR and, to our knowledge,
329 computational studies on long-term multiple follow-up cases that are able to report
330 the change of hemodynamic parameters have been lacking. Therefore, in the current
331 study, we investigate two patients showing similar physical and hemodynamic
332 features at initial presentation but presenting different FL development (stable in PI
333 and expanded in PII) during the follow-ups. We preliminarily identify the possible
334 hemodynamic parameters that could help to evaluate/predict FL enlargement and
335 thrombosis formation. In this study, the variation trends of the hemodynamic

336 parameters are more important than their absolute values.

337 The mechanical load acting on the FL boundary, which includes the outer wall of
338 FL and the flap, induces FL enlargement and at the same time restricts TL
339 remodeling. The pressure that is normally applied on the FL wall plays a key role in
340 luminal remodeling[34] and the local flow directly relates to its distribution and
341 magnitude. The flow can be assessed by its amount and the velocity. The first is
342 mainly related to the size of tears. By comparing Fig.4b~c and Table 1, it can be
343 found that the absolute flow mass passes each tear per second has positive relationship
344 with the size of the tear. This can be shown on AoT-3 of PI and AoT-2~3 of PII, since
345 they have multiple follow-up data, and it is consistent with previous report[14]. The
346 second, velocity, is determined by both the flow rate as well as the tear size; a smaller
347 tear size is correspondent to smaller flow rate yet accelerates the flow at the same
348 time. For instance, in the final two examinations of PI (PI-6 and PI-7), the amount of
349 the blood entering FL via AoT-3 decreases from 5.43% to 3.09% of the total flow and
350 the tear size decreases from 93.49mm² to 44.09mm². However, the flow passing this
351 tear has been accelerated and induces stronger impact on the FL outer wall (Fig.5e). If
352 studying a longer period (PI-4~7), the variation of W_{FL} at L3 (Fig.2e), where just
353 below AoT-3 in PI, is similar to the variation of the ratio between the diverted flow
354 amount and the tear size.

355 Along the aorta, the pressure in TL decreases generally but that in FL, due to the
356 vortical flow and its higher energy exchange, it does not present significant spatial
357 difference. The AoTs, functioning as the bridge between TL and FL, transport blood
358 flow and also pressure gradient. This induces similar pressure in the TL and FL near
359 the tears. Because of the relatively uniform P_{FL} and its connection with P_{TL} at the
360 tears, in general, P_{FL} is smaller than P_{TL} in the proximal region (above the AoTs) and
361 higher than P_{TL} in the downstream. This general distribution feature is shown in Fig.5
362 in all of the post-interventional cases at the moment of systolic peak and similar
363 patterns can be found in other time steps of the cardiac cycle.

364 At the flap, P_{FL} and P_{TL} conflict each other; the difference between them (PDiff)
365 may be associated with subsequent luminal remodeling[14]. Luminal remodeling is a
366 long-term effect; investigation of PDiff in short-term follow-ups may show the
367 variation trends of lumen remodeling, while PDiff in long-term follow-ups may be
368 consistent to lumen remodeling results. Indeed, taking L3 as an example, in short-term
369 (PI-2~3, PII-2~3), PD in PII increases from 1.44 to 2.93mmHg (7days-1month);

370 while, PDiff in PI remains about 0.55mmHg (7days-4month). This, earlier than
371 luminal change (Fig.2), shows the potential of FL enlargement for PII. In long-term
372 follow-ups (PI-4~7, PII-4~5), AoT-3 becomes the main FL flow entry in PI and
373 AoT-2 is the main entry in PII. PDiff increases from negative to positive slightly
374 below the position of AoT-3 in PI and AoT-2 in PII. Moreover, in both patients, in the
375 final examination, the maximum PDiff occurs near L3, where W_{FL} increases the most
376 (among the compared four positions) and W_{TL} in PII decreases. The abovementioned
377 indicates: (i) in short-term follow-ups, great increase of PDiff may imply potential FL
378 expansion; (ii) while, in long-term follow-up, the position of the first flow entry of FL
379 is the negative-to-positive watershed of PDiff, the position of the maximum PDiff is
380 consistent with the greatest W_{FL} increase, and when the maximum PDiff is small
381 (0.22mmHg in PI-7), the pressure induces slight FL expansion without restricted acts
382 on TL, but when it is relatively large (1.39mmHg in PII-5), both FL expansion and TL
383 collapse are found. In clinical examinations, monitoring PDiff at early-stage and
384 identifying the position of FL entries and the position of largest PDiff may assist in
385 wisely control of the untreated aorta segment.

386 The WSS is related to the formation of thrombosis. Previous studies suggested that
387 the tearing of the aortic wall and high WSS in the near region of the tears could
388 promote initial activation of platelets as well as the formation of platelet aggregates;
389 while, the highly vortical flow pattern in the FL corresponding with low WSS
390 promotes platelet aggregation and deposition, so that leads to surface thrombosis [35,
391 36]. In other words, lower WSS may induce surface thrombus and thus lead to
392 constructive FL remodeling [37, 38]. In the long-term follow-ups (PI-4~5 and
393 PII-4~5), complete thrombosis is found at the proximal region of dissection and
394 partial thrombosis remains above the re-entries. The partial thrombosis in both PI and
395 PII is aligned with the intimal flap; thus, WSS on the flap along the TL and FL sides
396 are compared. The WSS_{FL} is significantly lower than WSS_{TL} throughout the cardiac
397 cycle; the low WSS_{FL} possibly induces surface thrombus along the flap in FL while
398 the high WSS_{TL} can keep the TL patent. The lowest WSS_{FL} (<0.25Pa) occurs at the
399 proximal region of FL (Fig.7d), implying potential thrombosis in these regions.
400 Indeed, partial thrombosis in PI-4~5 with very low WSS_{FL} turns to complete
401 thrombosis in PI-6~7 (indicated by arrow in Fig.7d). Moreover, in PII, the WSS_{FL} at
402 the tip of the flap in PII-3 is small (<0.25Pa). In its next follow-up (PII-4), growth of
403 partial thrombosis can be found (indicated by arrow in Fig.7d). However, slightly

404 higher WSS_{FL} is shown in PII-4 at the proximal tip, and in its next follow-up (PII-5),
405 the partial thrombosis is slightly reduced (indicated by hollow arrow in Fig.7d). This
406 indicates the surface thrombosis is possibly very sensitive to WSS, and during the
407 long-term recovery, FL regression/growth could be repeatedly occurred at the
408 proximal tip of the FL.

409 The derived parameter of shear stress - RRT is related to particle residence and may
410 reflect thrombosis establishment as well[14]. To identify the location of high RRT,
411 Fig.8a~b draw the distribution of the normalized RRT to its maximum value in each
412 model. It shows that high RRT corresponds to the region with highly vortical and low
413 velocity flow. This occurs at the FL proximal tip for both the patients (PI-2~5,
414 PII-2~5). Moreover, Fig.8c compares the magnitude of RRT in PI-5 and PII-4, in
415 which the follow-up periods are similar (21 and 18months for PI and PII
416 respectively). The maximum RRT in PI-5 and PII-4 are 68.94 and $70.66Pa^{-1}$
417 respectively. The similar distribution pattern and magnitude of RRT in PI and PII
418 indicates that the values of RRT alone may not be able to predict FL remodeling. To
419 further investigate this, the variation of the maximum RRT is studied (Fig.8d). The
420 maximum RRTs in PI-3~7 and PII-3~5 are normalized to the correspondent first
421 follow-up results (PI-2 and PII-2, 7days post-TEVAR). The variation patterns of this
422 normalized maximum RRT show significant difference between PI and PII. This
423 implicates that, post-TEVAR, variation of RRT in short- to middle-term follow-up
424 (PI-2~5, PII-2~4) may play a key role in thrombosis establishment: an increase of
425 RRT after TEVAR and maintaining the relative normalized maximum RRT value to
426 be above 1.0 (Fig.8d) may lead to positive FL remodeling.

427 Common morphological predictors for re-intervention or surgery after TEVAR
428 include aortic diameter $>55mm$ and growth rate $>10mm/year$ [39]. Hemodynamic
429 condition of the dissected aorta plays an important role in driving TL and FL
430 remodeling. In other words, hemodynamic parameters may have the potential to
431 predict the dissection development earlier than morphological change. **However,**
432 **hemodynamic markers that can possibly predict FL development post-TEVAR have**
433 **not been proposed yet, which would require long-term multiple follow-up analyses.**
434 **The current study investigated the correlation of hemodynamic parameters to the**
435 **development of post-TEVAR dissection. It preliminarily proposed the parameters that**
436 **are potential to differentiate the enlarged and stable FL in an early stage post-TEVAR.**
437 **Although this study was based on a limited number of patient cases and thus no**

438 clinical conclusion can be drawn at this stage, it is the basis to future studies on a
439 larger amount of patient cases and would contribute to the research regarding early
440 decision-making on re-intervention or surgery for AoD after TEVAR.

441

442 **LIMITATIONS**

443 This study, based on long-term multiple follow-up data of two patients, preliminarily
444 shows the relationship of the variations between hemodynamic parameters and
445 luminal remodeling. However, critical values of these parameters should be better
446 determined by involving a greater number of patient cases. Besides, more detailed
447 mechanical analysis should involve the fluid-structure interaction analysis, which
448 does not only provide the stress information in the aortic wall but also offer more
449 accurate results on the WSS. However, due to the complex geometry and the lack of
450 the actual material properties, the existed fluid-structure interaction studies on AoD
451 often generate the aortic/dissection wall with arbitrary thickness and assume the
452 mechanical properties of the aortic and dissection wall similar to the properties of
453 aortic aneurysms. More accurate simulations are highly dependent on accurate model
454 establishment and material property measurements, which are currently carried on in
455 our laboratory.

456

457 **ACKNOWLEDGEMENTS**

458 This study was supported by National Natural Science Foundation of China
459 (81471752, 81353265), National Science and Technology Pillar Program of China
460 (2015BAI04B03), and National Key Research and Development Program of China
461 (2017YFC0107900). PW was partially supported by UK EPSRC (EP/N014642/1).

462

463 **CONFLICTS OF INTEREST**

464 No

465

466 **ETHICAL APPROVAL**

467 This study was approved by the Institutional Review Board of Chinese PLA General
468 Hospital (ref no. 20110903.V1.1)

469

470 REFERENCES

- 471 1. Younes, H.K., P.W. Harris, J. Bismuth, K. Charlton-Ouw, E.K. Peden, A.B. Lumsden, and M.G.
472 Davies, Thoracic endovascular aortic repair for type B aortic dissection. *Ann Vasc Surg* 2010;
473 24: p. 39-43.
- 474 2. Weber, T.F., D. Bockler, M. Muller-Eschner, M. Bischoff, M. Kronlage, H. von Tengg-Kobligk,
475 H.U. Kauczor, and A. Hyhlik-Durr, Frequency of abdominal aortic expansion after thoracic
476 endovascular repair of type B aortic dissection. *Vascular* 2016; 24: p. 567-79.
- 477 3. Doyle, B.J. and P.E. Norman, Computational Biomechanics in Thoracic Aortic Dissection:
478 Today's Approaches and Tomorrow's Opportunities. *Ann Biomed Eng* 2016; 44: p. 71-83.
- 479 4. Saad, A.A., T. Loupas, and L.G. Shapiro, Computer vision approach for ultrasound Doppler
480 angle estimation. *J Digit Imaging* 2009; 22: p. 681-88.
- 481 5. Muller-Eschner, M., F. Rengier, S. Partovi, R. Unterhinninghofen, D. Bockler, S. Ley, and H.
482 von Tengg-Kobligk, Tridirectional phase-contrast magnetic resonance velocity mapping
483 depicts severe hemodynamic alterations in a patient with aortic dissection type Stanford B. *J*
484 *Vasc Surg* 2011; 54: p. 559-62.
- 485 6. Stadlbauer, A., W. van der Riet, S. Globits, G. Crelier, and E. Salomonowitz, Accelerated
486 phase-contrast MR imaging: comparison of k-t BLAST with SENSE and Doppler ultrasound
487 for velocity and flow measurements in the aorta. *J Magn Reson Imaging* 2009; 29: p. 817-24.
- 488 7. Kohler, B., U. Preim, M. Grothoff, M. Gutberlet, K. Fischbach, and B. Preim, Motion-aware
489 stroke volume quantification in 4D PC-MRI data of the human aorta. *Int J Comput Assist*
490 *Radiol Surg* 2016; 11: p. 169-79.
- 491 8. Sakalihasan, N., C.A. Nienaber, R. Hustinx, P. Lovinfosse, M. El Hachemi, J.P. Chery-Bien,
492 L. Seidel, J.P. Lavigne, J. Quaniers, M.A. Kerstenne, A. Courtois, A. Ooms, A. Albert, J.O.
493 Defraigne, and J.B. Michel, (Tissue PET) Vascular metabolic imaging and peripheral plasma
494 biomarkers in the evolution of chronic aortic dissections. *Eur Heart J Cardiovasc Imaging* 2015;
495 16: p. 626-33.
- 496 9. Nchimi, A., J.P. Chery-Bien, T.C. Gasser, G. Namur, P. Gomez, L. Seidel, A. Albert, J.O.
497 Defraigne, N. Labropoulos, and N. Sakalihasan, Multifactorial relationship between
498 18F-fluoro-deoxy-glucose positron emission tomography signaling and biomechanical
499 properties in unruptured aortic aneurysms. *Circ Cardiovasc Imaging* 2014; 7: p. 82-91.
- 500 10. Alimohammadi, M., O. Agu, S. Balabani, and V. Diaz-Zuccarini, Development of a
501 patient-specific simulation tool to analyse aortic dissections: assessment of mixed
502 patient-specific flow and pressure boundary conditions. *Med Eng Phys* 2014; 36: p. 275-84.
- 503 11. Karmonik, C., M. Muller-Eschner, S. Partovi, P. Geisbusch, M.K. Ganten, J. Bismuth, M.G.
504 Davies, D. Bockler, M. Loebe, A.B. Lumsden, and H. von Tengg-Kobligk, Computational fluid
505 dynamics investigation of chronic aortic dissection hemodynamics versus normal aorta. *Vasc*
506 *Endovascular Surg* 2013; 47: p. 625-31.
- 507 12. Shang, E.K., D.P. Nathan, R.M. Fairman, J.E. Bavaria, R.C. Gorman, J.H. Gorman, 3rd, and
508 B.M. Jackson, Use of computational fluid dynamics studies in predicting aneurysmal
509 degeneration of acute type B aortic dissections. *J Vasc Surg* 2015; 62: p. 279-84.
- 510 13. Tse, K.M., P. Chiu, H.P. Lee, and P. Ho, Investigation of hemodynamics in the development of
511 dissecting aneurysm within patient-specific dissecting aneurysmal aortas using computational
512 fluid dynamics (CFD) simulations. *J Biomech* 2011; 44: p. 827-36.
- 513 14. Cheng, Z., N.B. Wood, R.G. Gibbs, and X.Y. Xu, Geometric and flow features of type B aortic
514 dissection: initial findings and comparison of medically treated and stented cases. *Ann Biomed*
515 *Eng* 2015; 43: p. 177-89.
- 516 15. Chen, D., M. Muller-Eschner, H. von Tengg-Kobligk, D. Barber, D. Bockler, R. Hose, and Y.
517 Ventikos, A patient-specific study of type-B aortic dissection: evaluation of true-false lumen
518 blood exchange. *Biomed Eng Online* 2013; 12: p. 65.
- 519 16. Karmonik, C., J. Bismuth, M.G. Davies, D.J. Shah, H.K. Younes, and A.B. Lumsden, A
520 computational fluid dynamics study pre- and post-stent graft placement in an acute type B
521 aortic dissection. *Vasc Endovascular Surg* 2011; 45: p. 157-64.
- 522 17. Cheng, S.W., E.S. Lam, G.S. Fung, P. Ho, A.C. Ting, and K.W. Chow, A computational fluid
523 dynamic study of stent graft remodeling after endovascular repair of thoracic aortic dissections.
524 *J Vasc Surg* 2008; 48: p. 303-9.
- 525 18. Chen, D., M. Muller-Eschner, D. Kotelis, D. Bockler, Y. Ventikos, and H. von Tengg-Kobligk,

526 A longitudinal study of Type-B aortic dissection and endovascular repair scenarios:
527 computational analyses. *Med Eng Phys* 2013; 35: p. 1321-30.

528 19. Karmonik, C., J. Bismuth, D.J. Shah, M.G. Davies, D. Purdy, and A.B. Lumsden,
529 Computational study of haemodynamic effects of entry- and exit-tear coverage in a DeBakey
530 type III aortic dissection: technical report. *Eur J Vasc Endovasc Surg* 2011; 42: p. 172-7.

531 20. Naim, W.N.W.A., P. Ganesan, Z. Sun, K. Osman, and E. Lim, The impact of the number of
532 tears in patient-specific stanford type B aortic dissecting aneurysm: CFD simulations. *J Mech*
533 *Med Biol* 2014; 14: p. 1450017.

534 21. Alimohammadi, M., J.M. Sherwood, M. Karimpour, O. Agu, S. Balabani, and V.
535 Diaz-Zuccarini, Aortic dissection simulation models for clinical support: fluid-structure
536 interaction vs. rigid wall models. *Biomed Eng Online* 2015; 14: p. 34.

537 22. Qiao, A., W. Yin, and B. Chu, Numerical simulation of fluid-structure interaction in bypassed
538 DeBakey III aortic dissection. *Comput Methods Biomech Biomed Engin* 2015; 18: p. 1173-80.

539 23. Clough, R.E., V.E. Zymvragoudakis, L. Biasi, and P.R. Taylor, Usefulness of new imaging
540 methods for assessment of type B aortic dissection. *Ann Cardiothorac Surg* 2014; 3: p. 314-8.

541 24. Birjiniuk, J., J.M. Ruddy, E. Iffrig, T.S. Henry, B.G. Leshnower, J.N. Oshinski, D.N. Ku, and
542 R.K. Veeraswamy, Development and testing of a silicone in vitro model of descending aortic
543 dissection. *J Surg Res* 2015; 198: p. 502-7.

544 25. Soudah, E., P. Rudenick, M. Bordone, B. Bijmens, D. Garcia-Dorado, A. Evangelista, and E.
545 Onate, Validation of numerical flow simulations against in vitro phantom measurements in
546 different type B aortic dissection scenarios. *Comput Methods Biomech Biomed Engin* 2015; 18:
547 p. 805-15.

548 26. Vignon-Clementel, I.E., C.A. Figueroa, K.E. Jansen, and C.A. Taylor, Outflow boundary
549 conditions for three-dimensional finite element modeling of blood flow and pressure in arteries.
550 *Comput Methods Biomech Biomed Engin* 2006; 195: p. 3776-96.

551 27. Ganten, M.K., T.F. Weber, H. von Tengg-Kobligk, D. Bockler, W. Stiller, P. Geisbusch, G.W.
552 Kauffmann, S. Delorme, M. Bock, and H.U. Kauczor, Motion characterization of aortic wall
553 and intimal flap by ECG-gated CT in patients with chronic B-dissection. *Eur J Radiol* 2009; 72:
554 p. 146-53.

555 28. Papaharilaou, Y., D.J. Doorly, and S.J. Sherwin, The influence of out-of-plane geometry on
556 pulsatile flow within a distal end-to-side anastomosis. *J Biomech* 2002; 35: p. 1225-39.

557 29. Bortolotto, L.A. and M.E. Safar, Blood pressure profile along the arterial tree and genetics of
558 hypertension. *Arq Bras Cardiol* 2006; 86: p. 166-9.

559 30. Gorring, N., L. Kark, A. Simmons, and T. Barber, Determining possible thrombus sites in an
560 extracorporeal device, using computational fluid dynamics-derived relative residence time.
561 *Comput Methods Biomech Biomed Engin* 2015; 18: p. 628-34.

562 31. Nienaber, C.A., S. Kische, H. Ince, and R. Fattori, Thoracic endovascular aneurysm repair for
563 complicated type B aortic dissection. *J Vasc Surg* 2011; 54: p. 1529-1533.

564 32. Andacheh, I.D., C. Donayre, F. Othman, I. Walot, G. Kopchok, and R. White, Patient outcomes
565 and thoracic aortic volume and morphologic changes following thoracic endovascular aortic
566 repair in patients with complicated chronic type B aortic dissection. *J Vasc Surg* 2012; 56: p.
567 644-50.

568 33. Sigman, M.M., O.P. Palmer, S.W. Ham, M. Cunningham, and F.A. Weaver, Aortic morphologic
569 findings after thoracic endovascular aortic repair for type B aortic dissection. *JAMA Surg* 2014;
570 149: p. 977-83.

571 34. Sueyoshi, E., I. Sakamoto, K. Hayashi, T. Yamaguchi, and T. Imada, Growth rate of aortic
572 diameter in patients with type B aortic dissection during the chronic phase. *Circulation* 2004;
573 110: p. II256-61.

574 35. Sheriff, J., D. Bluestein, G. Girdhar, and J. Jesty, High-shear stress sensitizes platelets to
575 subsequent low-shear conditions. *Ann Biomed Eng* 2010; 38: p. 1442-50.

576 36. Goel, M.S. and S.L. Diamond, Adhesion of normal erythrocytes at depressed venous shear
577 rates to activated neutrophils, activated platelets, and fibrin polymerized from plasma. *Blood*
578 2002; 100: p. 3797-803.

579 37. Wu, M.H., Y. Kouchi, Y. Onuki, Q. Shi, H. Yoshida, S. Kaplan, R.F. Viggers, R. Ghali, and L.R.
580 Sauvage, Effect of differential shear stress on platelet aggregation, surface thrombosis, and
581 endothelialization of bilateral carotid-femoral grafts in the dog. *J Vasc Surg* 1995; 22: p.
582 382-90.

- 583 38. Menichini, C., Z. Cheng, R.G. Gibbs, and X.Y. Xu, Predicting false lumen thrombosis in
584 patient-specific models of aortic dissection. *J R Soc Interface* 2016; 13: p. 20160759.
- 585 39. Erbel, R., V. Aboyans, C. Boileau, E. Bossone, R.D. Bartolomeo, H. Eggebrecht, A.
586 Evangelista, V. Falk, H. Frank, O. Gaemperli, M. Grabenwoger, A. Haverich, B. Iung, A.J.
587 Manolis, F. Meijboom, C.A. Nienaber, M. Roffi, H. Rousseau, U. Sechtem, P.A. Sirnes, R.S.
588 Allmen, and C.J. Vrints, 2014 ESC Guidelines on the diagnosis and treatment of aortic diseases:
589 Document covering acute and chronic aortic diseases of the thoracic and abdominal aorta of
590 the adult. The Task Force for the Diagnosis and Treatment of Aortic Diseases of the European
591 Society of Cardiology (ESC). *Eur Heart J* 2014; 35: p. 2873-926.
- 592

FIGURE LEGENDS

- Fig.1** (a)~(d) display the reconstructed models of AoD (D-days, M-months); (e) is a sonogram of Doppler ultrasound velocimetry, the upper edge of which is shown in green; (f) shows an axial slice of CTA scan at initial presentation of PI, in which the segmented lumen boundary is shown in yellow.
- Fig.2** The luminal remodeling. (a) displays the measured axial positions (L1-4) and the regions to calculate luminal volume (V_{TL} , V_{TL} -Part and V_{FL}); (b)~(e) show the variation of luminal volume, aortic diameter, width of TL and FL respectively.
- Fig.3** Flow patterns of AoD. (a)~(b) display the flow streamlines at systolic peak; (c) shows the streamlines at the proximal region of FL in the final model of PII.
- Fig.4** Flow exchange between the true and false lumen. (a) displays the variation of the mass flow rate towards the FL via the primary entry, AoT-2 and AoT-3 over a cardiac cycle at initial presentation; (b) and(c) respectively show the mass flow rate variation at AoT-2 and AoT-3 during the longitudinal follow-ups.
- Fig.5** Pressure distribution along the dissected aorta. (a) and (b) display the PDsys distribution in PI and PII respectively; (c) shows the PDsys in a normal aorta; (d) displays the variation of the maximum PDsys during the follow-up; (e) shows the Psys at a slice crossing the FL in the final two examinations of PI and in the final examination of PII; and (f) shows the region with $P_{sys} \geq 99.15\text{mmHg}$ (in red).
- Fig.6** Pressure difference between FL and TL for PI (a)~(d) and PII (e)~(f).
- Fig.7** WSS distribution along the flap. (a) and (b) display the WSS distribution at systolic peak on the flap of TL and FL side respectively; (c) and (d) show the WSS distribution on the flap of FL side during the long-term follow-ups in different WSS ranges.
- Fig.8** RRT distribution and variation. (a) and (b) show the normalized RRT to its maximum value post-TEVAR in PI and PII respectively; (c) shows the RRT distribution at PI-5 and PII-4, where the follow-up periods in PI and PII are similar; and (d) displays the variation of the normalized maximum RRT to its value in the first follow-up (PI-2 for PI and PII-2 for PII).

FIGURE 1

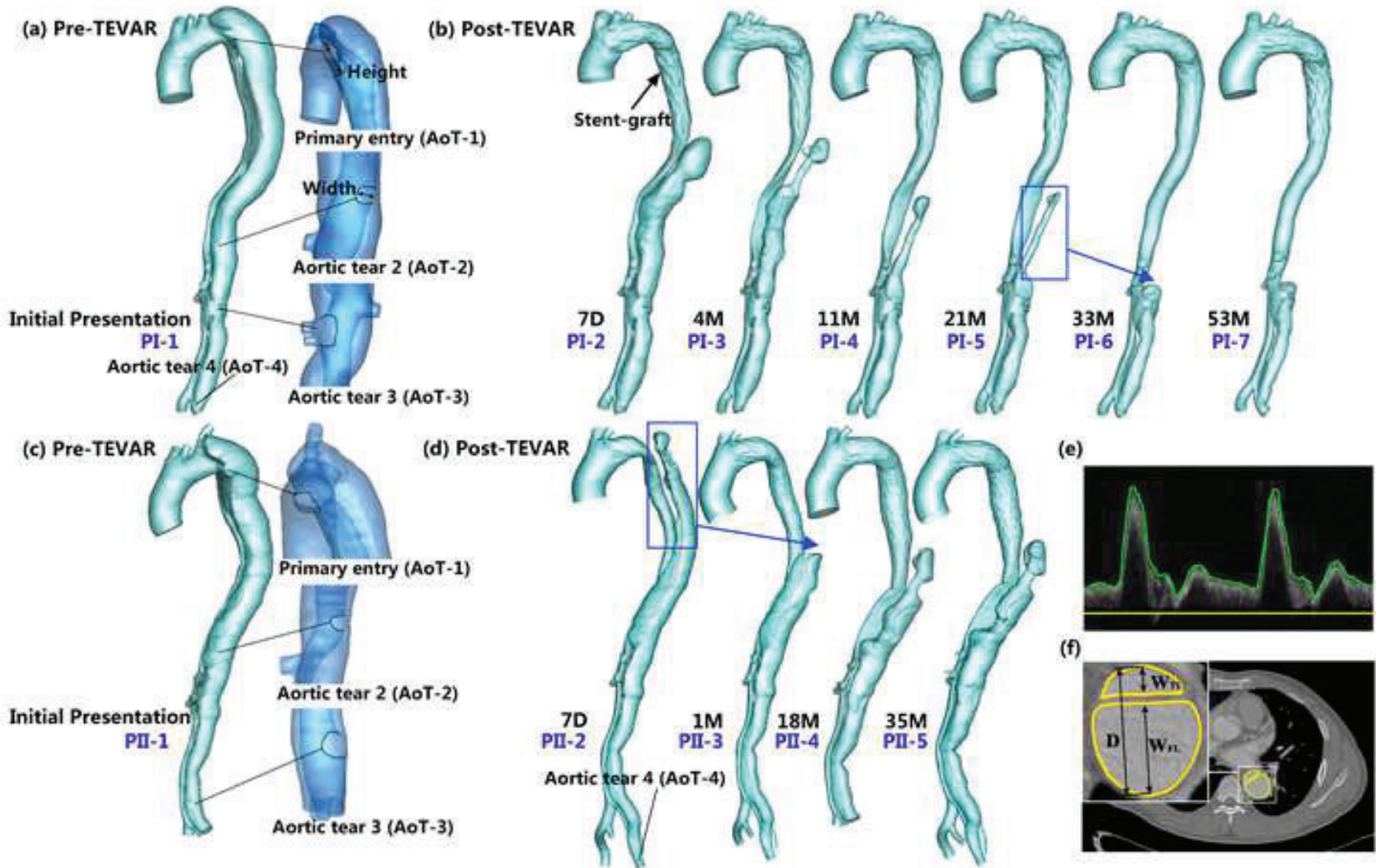


Figure 2

[Click here to download high resolution image](#)

FIGURE 2

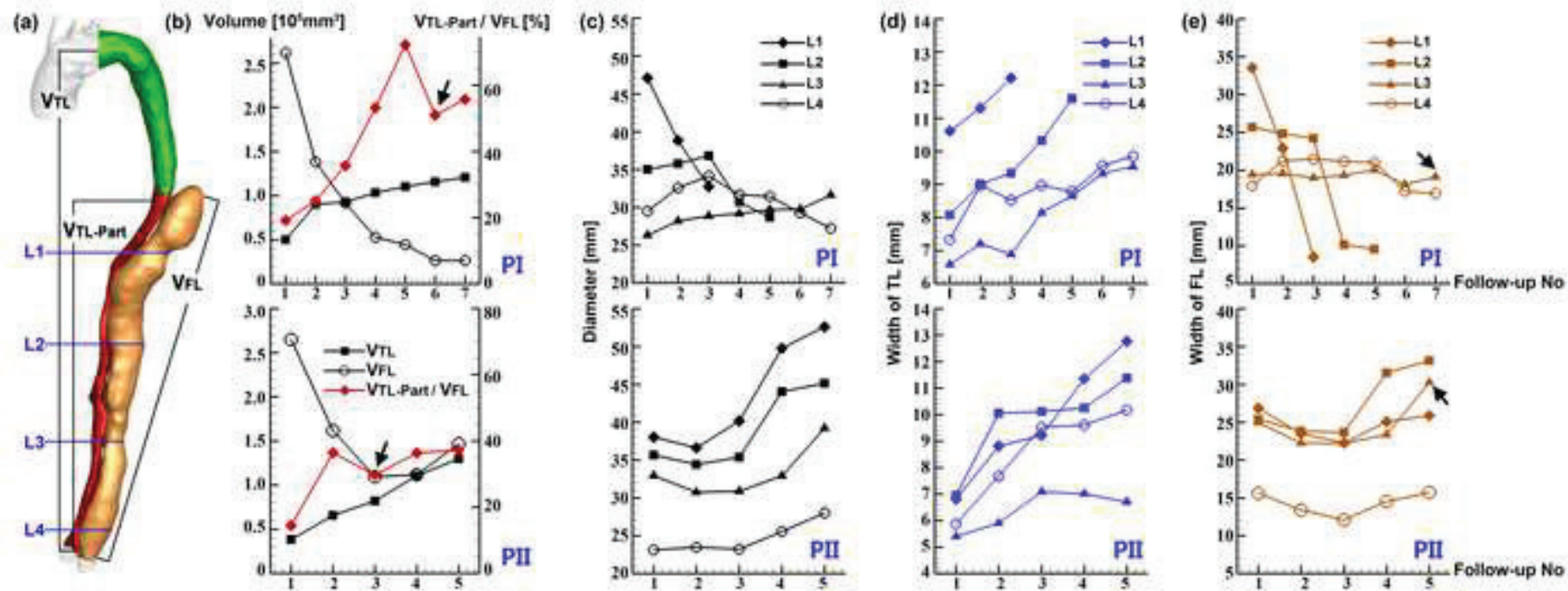


FIGURE 3

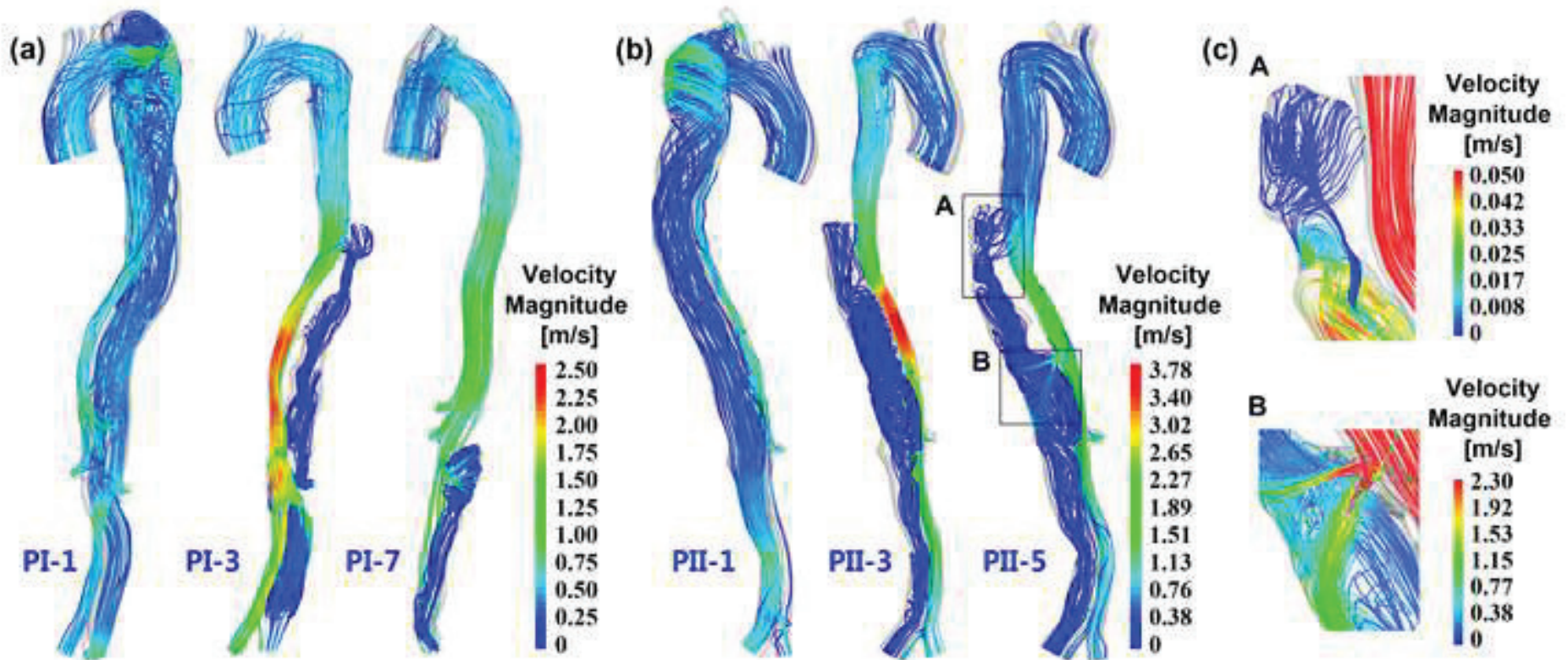


Figure 4

[Click here to download high resolution image](#)

FIGURE 4

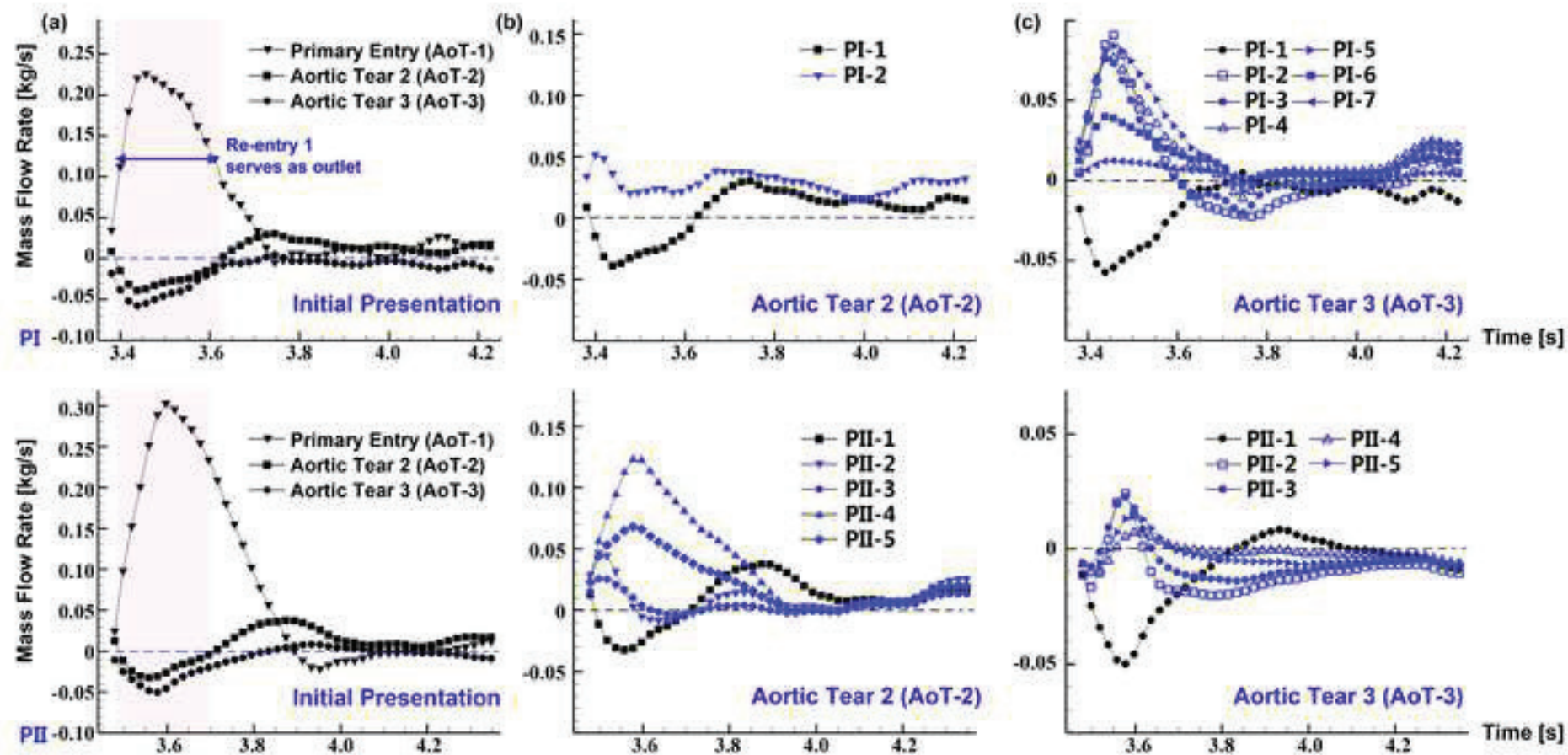


FIGURE 5

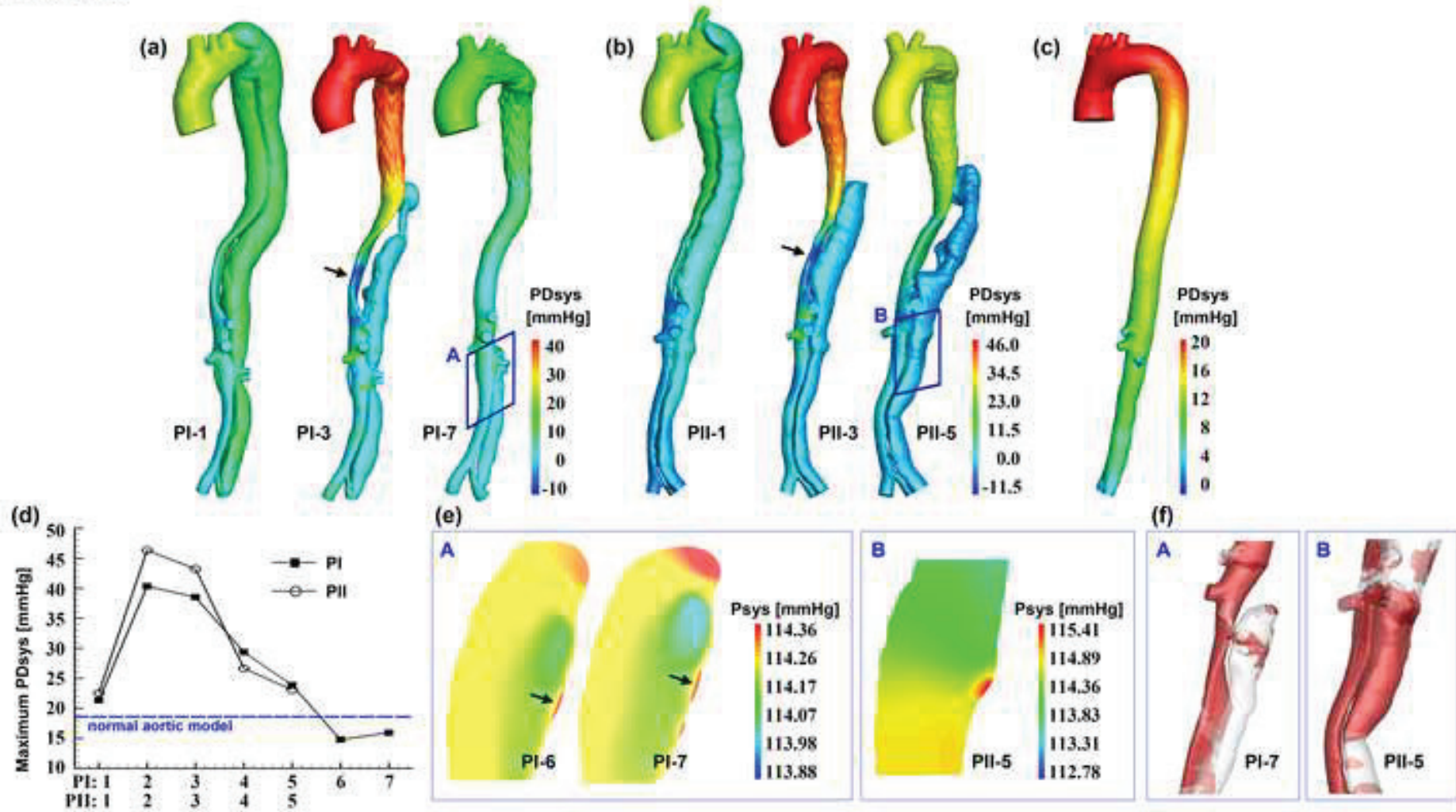


FIGURE 6

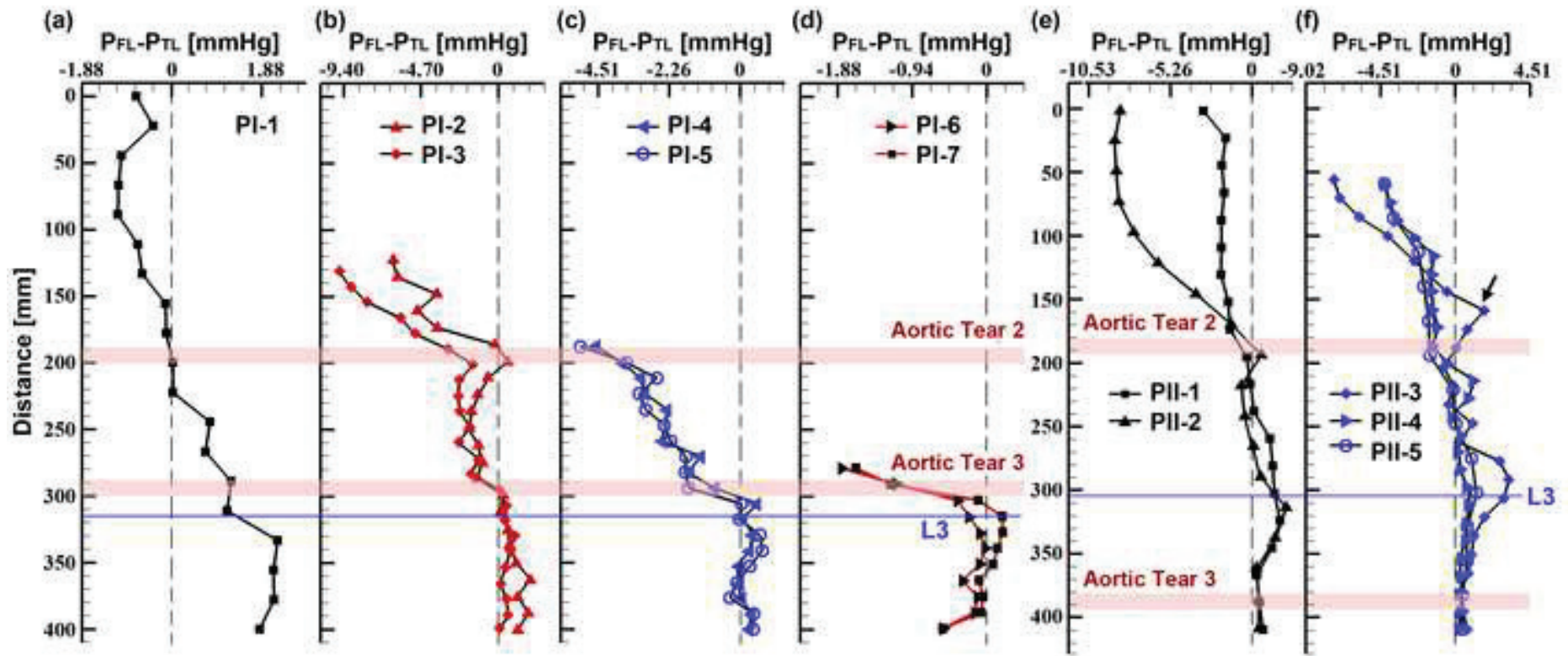


Figure 7
[Click here to download high resolution image](#)

FIGURE 7

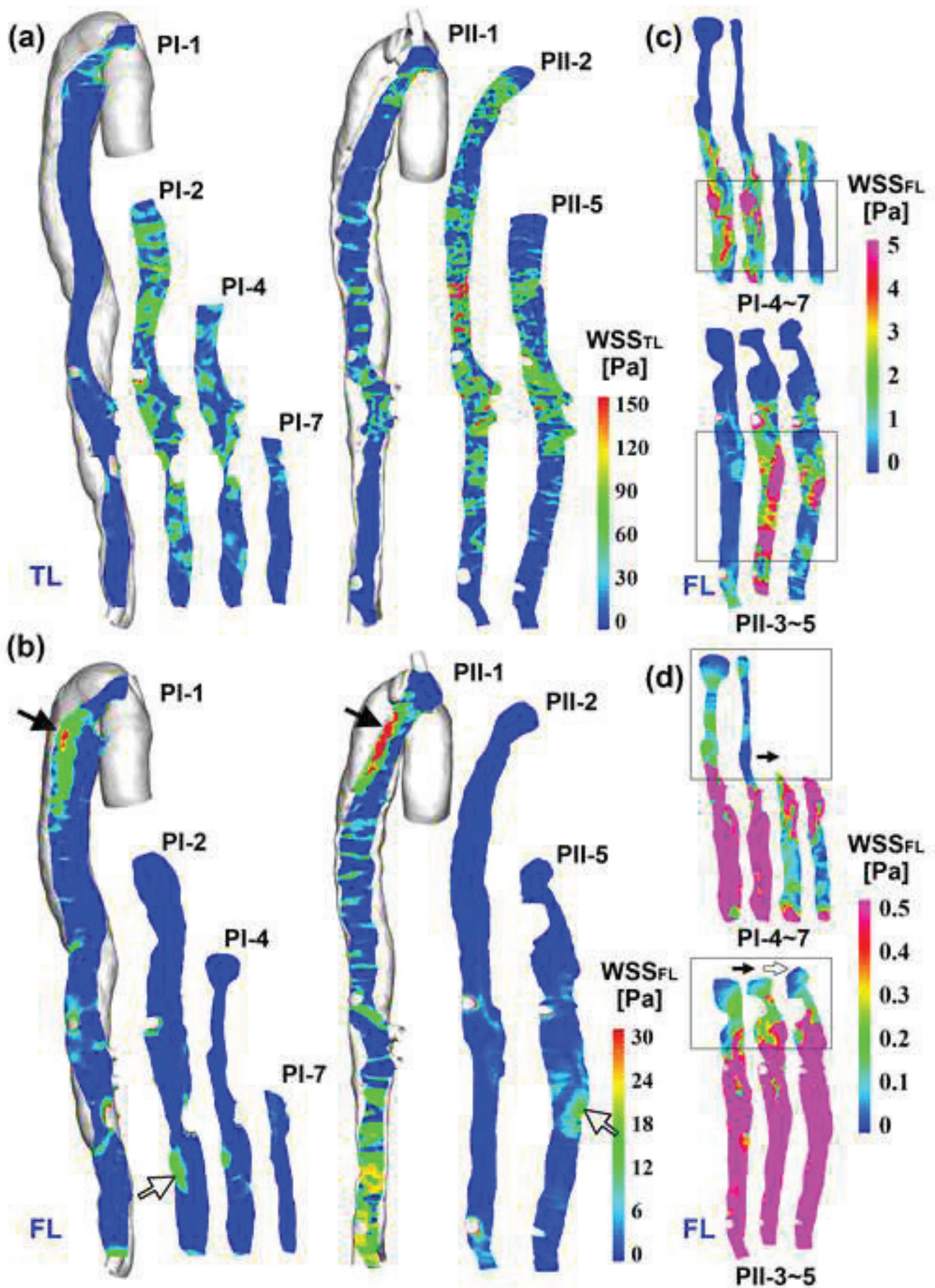
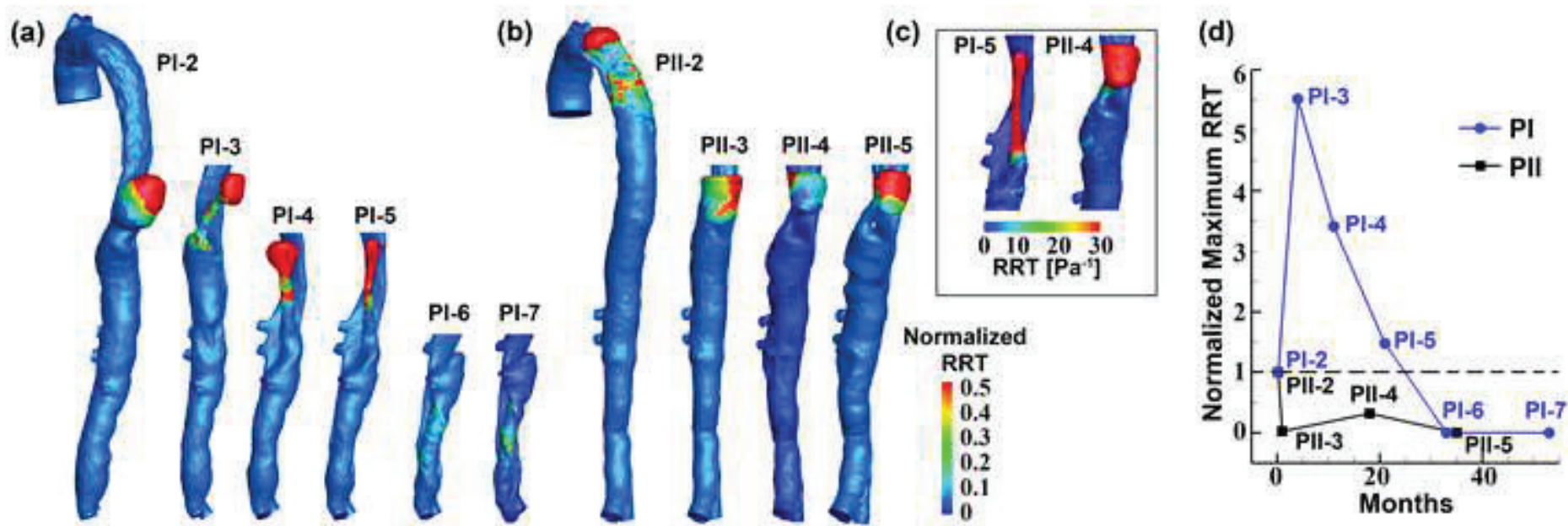


Figure 8

[Click here to download high resolution image](#)

FIGURE 8



Supplementary data

[Click here to download Supplementary data: Supplement-revision.docx](#)

Supplementary Video 1

[Click here to download Supplementary data: SupplementaryVideoS1.gif](#)

Supplementary Video 2

[Click here to download Supplementary data: SupplementaryVideoS2.gif](#)

Supplementary Video 3

[Click here to download Supplementary data: SupplementaryVideoS3.gif](#)

Supplementary Video 4

[Click here to download Supplementary data: SupplementaryVideoS4.gif](#)

Supplementary Video 5

[Click here to download Supplementary data: SupplementaryVideoS5.gif](#)

Supplementary Video 6

[Click here to download Supplementary data: SupplementaryVideoS6.gif](#)